Title	Development of a mesoscopic framework spanning nanoscale protofibril dynamics to macro-scale fibrin clot formation
Author(s)	Takeishi, Naoki; Shigematsu, Taiki; Enosaki, Ryogo et al.
Citation	Journal of the Royal Society Interface. 2021, 18(184), p. 20210554
Version Type	VoR
URL	https://hdl.handle.net/11094/88626
rights	This article is licensed under a Creative Commons Attribution 4.0 International License.
Note	

INTERFACE

Research

Author for correspondence:
Satoshi Ii
e-mail: sii@tmu.ac.jp

THE ROYAL SOCIETY
PUBLISHING

Development of a mesoscopic framework spanning nanoscale protofibril dynamics to macro-scale fibrin clot formation

Naoki Takeishi[1], Taiki Shigematsu[1], Ryogo Enosaki[1], Shunichi Ishida[2], Satoshi Ii[3] and Shigeo Wada[1]

[1]Graduate School of Engineering Science, Osaka University, 1-3 Machikaneyama Toyonaka, Osaka 560-8531, Japan
[2]Graduate School of Engineering, Kobe University, 1-1 Rokkodai, Nada, Kobe, 657-8501, Japan
[3]Graduate School of Systems Design, Tokyo Metropolitan University, 1-1 Minami-Osawa Hachioji, Tokyo 192-0397, Japan

SI, 0000-0002-5428-5385

Thrombi form a micro-scale fibrin network consisting of an interlinked structure of nanoscale protofibrils, resulting in haemostasis. It is theorized that the mechanical effect of the fibrin clot is caused by the polymeric protofibrils between crosslinks, or to their dynamics on a nanoscale order. Despite a number of studies, however, it is still unknown, how the nanoscale protofibril dynamics affect the formation of the macro-scale fibrin clot and thus its mechanical properties. A mesoscopic framework would be useful to tackle this multi-scale problem, but it has not yet been established. We thus propose a minimal mesoscopic model for protofibrils based on Brownian dynamics, and performed numerical simulations of protofibril aggregation. We also performed stretch tests of polymeric protofibrils to quantify the elasticity of fibrin clots. Our model results successfully captured the conformational properties of aggregated protofibrils, e.g., strain-hardening response. Furthermore, the results suggest that the bending stiffness of individual protofibrils increases to resist extension.

1. Introduction

Fibrin clots are one of dominant components of thrombi (others are, e.g. red cells or platelets), which play a crucial role in events such as haemostasis [1] and pulmonary thromboembolism [2]. Studies of fibrin clots have been conducted to clarify both physiological and pathological significance [1,3]. Particular attention has been paid to multi-scale spatiotemporal processes connecting the small components of fibrin clots (e.g. fibrinogen) to macro-scale thrombi [4–7]. Fibrin clots themselves consist of components on multiple scales. Each clot, over several microns in size, is the product of protofibril aggregation mediated by fibrinogen, which is a nano-scale 45-nm-long plasma protein consisting of six paired polypeptide chains (two pairs each of Aα-chains, Bβ-chains and γ-chains) [8–10]. Fibrinogen is activated by thrombin and polymerizes into a double-stranded fibre, the so-called protofibril [1,10]. Architecturally, the protofibril is a regularly repeating 22.5-nm unit corresponding to one-half the length of the fibrinogen protein [10–12].

Since a fibrin clot is an interlinked, branching structure consisting of protofibrils [13], it is expected that clot elasticity can result from the reaction of the polymeric filaments between cross-links, from alterations in the network structure, or both [7,14]. Researchers have shown that the mechanical properties of the fibrin network structure are altered by chemical and mechanical conditions (e.g. fibrinogen concentrations and the solvent flow field) [6,13,15,16]. For instance, it is well known that factor XIIIa increases the elasticity of individual
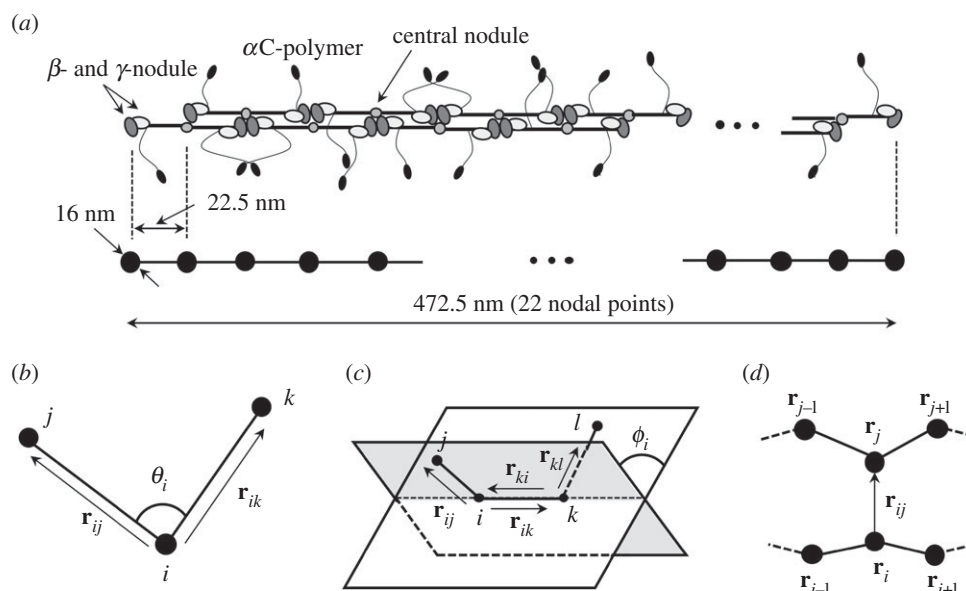
Figure 1. (a) Schematic of a protofibril model with length 472.5 nm, consisting of 22 nodal points in each 22.5-nm-long segment (node to node). Schematic images of (b) bending, (c) torsion and (d) aggregation energy, where superscript (·) represents two adjacent protofibrils.

fibrin fibres [17], thereby enhancing the stability of clots by increasing their stiffness and resistance against deformation [13,18,19]. It is also known that some medications commonly used to prevent and treat cardiovascular diseases (e.g. aspirin and heparin) affect fibrin polymerization and clot structure, making fibrin more porous, permeable, and susceptible to lysis [20,21]. Piechocka *et al.* [22] recently showed that γ-chain cross-linking contributes to clot elasticity by changing the force-extension behaviour of protofibrils, whereas α-chain cross-linking stiffens the clot, as a consequence of tighter coupling between the constituent protofibrils [22]. Despite a number of studies of fibrin clot formation, much is still unknown, in particular about how nanoscale protofibril dynamics affect macro-scale fibrin clot formation and then clot mechanical properties. Considering that the clotting time (or gel point) has been used in clinical assays as an indication of altered coagulation, understanding the mechanisms of fibrin polymerization may provide a basis for informative diagnostic tools, such as molecular markers of thrombin generation and intravascular fibrin deposition.

To comprehensively investigate the fibrin clot architecture and its mechanical properties, Onck *et al.* [23] numerically investigated the dynamics of individual (actin) fibrous components under shear flow using a two-dimensional model, and showed that stiffening of non-affine, cross-linked semiflexible networks is caused by the transition of a bending-dominated response at small strains to a stretching-dominated response at large strain [23]. Moiseyev *et al.* [24] used a theoretical and statistical model of fibrin clot growth to quantify the relationship between the density of fibre cross-linking and clot elasticity [24]. These models, however, cannot fully deal with the dynamics of fibrin clot components. Yesudasan *et al.* proposed the coarse-grained molecular dynamics model to investigate the complex network of fibrin clots [25,26]. However, the model focuses on the dynamics of fibrinogen molecules on a scale of several hundreds nanometres, whereas the network structures of fibrin clots on the scale of several micrometres, corresponding to the cellular scale level, have not yet been fully described.

A mesoscopic framework is needed to clarify the spatio-temporal relationship between the nanoscale protofibril behaviours and the mechanical properties of micrometre-scale fibrin clots, but no such framework has been established yet. Therefore, the objective in this study was to develop a framework to investigate fibrin clot formation on multiple scales, with a focus on nanoscale protofibrils behaviour. We proposed a minimal mesoscopic model for protofibrils based on Brownian dynamics. Using this model, we performed simulations of protofibril aggregation. For these polymeric protofibrils, we also performed numerical stretch tests to quantify the elasticity of fibrin clots. Based on these numerical approaches, we discuss the feasibility of a proposed model to study the multi-scale relationship between protofibril molecular dynamics and the mechanical response of fibrin clots.

2. Methods

2.1. Coarse-grain protofibril model

We consider the dynamics of protofibrils with a length of 472.5 nm in a static medium. Based on electron microscope observations [19], each protofibril is modelled as 22 nodal points in series, where the length of the segment consisting of two nodal points is set to 22.5 nm [11], which is the half the length of the 45-nm-long fibrinogen molecule [27]. The model schematic is shown in figure 1(a). Each nodal point is governed by the following overdamped Langevin equation:

$$c\frac{\partial \mathbf{r}_i}{\partial t} = -\frac{\partial W}{\partial \mathbf{r}_i} + \mathbf{F}_i^{\mathrm{rand}}, \quad (2.1)$$

where $\mathbf{r}_i$ is the position of the ith node, W is the total potential energy in the computational domain, $\mathbf{F}_i^{\mathrm{rand}}$ is the random force of the ith node, characterized as thermal fluctuations of solvent molecules and c is the frictional coefficient estimated by Stokes' Law, i.e. $c = 6\pi\mu a$. Here, μ (= 1.2 mPa · s) is the solvent viscosity of human plasma. Based on transmission electron microscopy, atomic force microscopy (AFM) and X-ray crystallographic data, the fibrinogen molecule is approximately 2–7 nm in

diameter [28–31]. Recent experimental observations using AFM reported that the length of γ-nodule is 5 nm in the naturally folded state (i.e. force-free condition). Considering a double-stranded fibre of protofibril [1,10], we define the characteristic radius of fibrinogen as 8 nm.

In this study, the total potential energy W is expressed as five different components, specifically stretch W^S, bend W^B, torsion W^T, aggregation W^A and repulsive energy W^R

$$W = W^S + W^B + W^T + W^A + W^R. \tag{2.2}$$

The stretch energy W^S and stretch force $\mathbf{f}_i^S$ of the ith node can be expressed as

$$W^S = \sum_{ij} \frac{k^S}{2}(|\mathbf{r}_{ij}| - \mathbf{r}_0^S)^2, \tag{2.3a}$$

$$\mathbf{f}_i^S = -\frac{\partial W^S}{\partial \mathbf{r}_i} = k^S(|\mathbf{r}_{ij}| - \mathbf{r}_0^S)\frac{\mathbf{r}_{ij}}{|\mathbf{r}_{ij}|} \tag{2.3b}$$

and

$$\mathbf{r}_{ij} = \mathbf{r}_j - \mathbf{r}_i, \tag{2.3c}$$

where k^S is the stretch energy constant, $\mathbf{r}_0^S$ (= 22.5 nm) is the reference length, which is half the length of the fibrinogen molecule [11], and $\mathbf{r}_j$ is the jth node adjacent to the ith node in the same protofibril. From both AFM experiments and molecular dynamics simulations, the stretch energy constant can be estimated from the extension dynamics of a single fibrinogen molecule [10,32]. For instance, Lim et al. [32] estimated the longitudinal spring constant of protofibrils as $O(k^S) \sim 10^{-3} \, \text{N m}^{-1}$ [32]. While in more recent coarse-grained molecular simulations by Tan et al. [33], the force constant for neighbouring bonds corresponding to k^S in this study, was set to be 250 kJ mol^{-1} Å^{-2}, which can be rewritten as 0.42 N m^{-1} [33]. Hence, in this study, we set as $k^S = 0.01 \, \text{N m}^{-1}$.

The bending energy W^B and bending force $\mathbf{f}_i^B$ of the ith node between the jth and kth nodes can be expressed as

$$W^B = \sum_{ijk} \frac{k^B}{2}(\theta_{ijk} - \theta_0)^2, \tag{2.4a}$$

$$\theta_{ijk} = \arccos\left(\frac{\mathbf{r}_{ij} \cdot \mathbf{r}_{ik}}{|\mathbf{r}_{ij}||\mathbf{r}_{ik}|}\right) \tag{2.4b}$$

and

$$\mathbf{f}_i^B = -\frac{\partial W^B}{\partial \mathbf{r}_i}, \tag{2.4c}$$

where k^B is the bending energy constant, θ_{ijk} is the angle at the ith node between the jth and kth nodes (figure 1b), and θ_0 (=π) is the reference angle [10]. In previous coarse-grained molecular dynamics simulations by [25,33], the bending energy constant was used in the range between 10^{-19} and 10^{-17} J rad^{-2}. Hence, in this study, the bending energy constant is set as $k^B = 0.1–10 \times 10^{-18}$ J rad^{-2}. The final form of equation (2.4c) is described in appendix A.

The torsion energy W^T and torsion force $\mathbf{f}_i^T$ of the ith node can be expressed as

$$W^T = \sum_{ijkl} \frac{k^T}{2}(\phi_i - \phi_0)^2 \tag{2.5a}$$

$$\phi_i = \text{sgn}\{\mathbf{r}_{jk} \cdot (\mathbf{m} \times \mathbf{n})\}\arccos\left(\frac{\mathbf{m} \cdot \mathbf{n}}{|\mathbf{m}||\mathbf{n}|}\right) \tag{2.5b}$$

and

$$\mathbf{f}_i^T = -\frac{\partial W^T}{\partial \mathbf{r}_i}, \tag{2.5c}$$

where k^T is the torsion energy constant, ϕ_i is the torsion angle (or dihedral angle) of the ith node among the jth, kth and lth nodes (figure 1c), ϕ_0 (=0) is the reference torsion angle, and $\mathbf{m}$ and $\mathbf{n}$ are the normal vectors, which are defined by four adjacent nodes on two planes (figure 1c)

$$\mathbf{m} = \mathbf{r}_{ij} \times \mathbf{r}_{ik} \tag{2.6a}$$

and

$$\mathbf{n} = \mathbf{r}_{ki} \times \mathbf{r}_{kl}. \tag{2.6b}$$

The final forms of equation (2.5c) at each of the four nodes are described in the appendix A. In previous coarse-grained modelling for DNA [34] and biomoleculars [33], the energy constant in equation (2.5) was considered in the range between 10^{-23}–10^{-21} J rad^{-2}. Although tightly coupled studies between experiment and simulation are needed to identify the value of the constant, the torsion energy constant k^T was set as $k^T = 1.0 \times 10^{-23}$ J rad^{-2} in this study.

Two protofibrils are bound to each other at the αC regions [1], and hence we define the aggregation force applied to two nodal points of different protofibrils, within a threshold a_{th} (= $2\mathbf{r}_0^S$), corresponding to the length of the fibrinogen molecule [11]. Considering two adjacent nodal points of different protofibrils (see figure 1d), the aggregation energy W^A and aggregation force $\mathbf{f}_i^A$ of the ith node can be written as

$$W^A = \sum_{ij} \frac{k^A}{2}(|\mathbf{r}_{ij}| - \mathbf{r}_0^A)^2, \tag{2.7a}$$

$$\mathbf{f}_i^A = -\frac{\partial W^A}{\partial \mathbf{r}_i} = -k^A(|\mathbf{r}_{ij}| - \mathbf{r}_0^A)\frac{\mathbf{r}_{ij}}{|\mathbf{r}_{ij}|} \tag{2.7b}$$

and

$$\mathbf{f}_j^A = -\mathbf{f}_i^A, \tag{2.7c}$$

where k^A is the aggregation energy constant and $\mathbf{r}_0^A$ (=$2a$) is the reference length between two adjacent nodes that are not present on the same protofibril. For simplicity, W^A is modelled as a simple harmonic potential form as shown in equation (2.7a). The formation could be written in light of the fact that lateral aggregation of protofibrils is responsible for local (several nanometre-scale) conformational changes [35], but this is beyond the scope of the present work. Instead of aggregation force constant between two fibrinogen, molecular interaction between platelet glycoprotein receptor GPIIb/IIIa (integrin $\alpha_{IIb}\beta_3$) and fibrinogen have been well investigated. For instance, Litvinov et al. (2011) experimentally investigated thermodynamics and kinetics of bonds between GPIIb/IIIa and fibrinogen, where the molecular spring (or aggregation) constant was used as 12 pN nm^{-1} (= 0.12 N m^{-1}) to estimate the energy needed to dissociate $\alpha_{IIb}\beta_3$ from fibrinogen in the long-duration state [36]. While in simulation work by [37], platelet adhesion and aggregation were modelled focusing on the interaction between the GPIIb/IIIa and its ligand, where the aggregation force constant for binding between GPIIb/IIIa and fibrinogen was set to as $k^A = 1.0 \times 10^{-4}$ N m^{-1}. According to those studies, the aggregation energy constant was set as $k^A = 0.2–20 \times 10^{-3}$ N m^{-1}.

Short distance between two charged particles leads to 'bouncing off', resulting in repulsive forces between the two, which corresponds to charged particles interacting through colloidal forces at constant surface charge. Several potential models have been proposed to represent such near-field dynamics, and the Lennard–Jones potential is one of the most classical and well-known models. This was also applied to previous coarse-grained molecular dynamics simulations of protofibrils, e.g. by [25,26]. In this study, however, we focus on developing a minimal mesoscopic model for protofibrils, and hence a non-hydrodynamic inter-node repulsive force is modelled as a simple linear function of two-nodes distance, which is defined only when the two node points on different protofibrils are within the diameter of the fibrinogen (=$2a$). This force practically allows us to avoid the prohibitively small time step needed to overcome the problem of overlapping nodes on different protofibrils. The repulsive energy W^R and repulsive force $\mathbf{f}_i^R$ of the ith node can be

Table 1. Nomenclature for the parameters and variables.

symbol	physical meaning	values (dimension)	reference
a	fibrinogen radius	8 nm	[42,43]
r_0^S	reference stretch length	22.5 nm	[11]
a_{th}	threshold of aggregation length	$2r_0^S$	—
r_0^A	reference aggregation length	$2a$	—
r_0^R	reference repulsive length	$2a$	—
θ_0	reference bending angle	π	[10]
ϕ_0	reference torsion angle	0	—
k_b	Boltzmann constant	1.38×10^{-23} J K^{-1}	—
T	temperature	300 K	—
k^A	aggregation energy constant	0.2–20×10^{-3} N m^{-1}	[36,37]
k^B	bending energy constant	0.1–10×10^{-18} J rad^{-2}	[25,33]
k^R	repulsive energy constant	1.0×10^{-3} N m^{-1}	—
k^S	stretch energy constant	0.01 N m^{-1}	[10,32,33]
k^T	torsion energy constant	1.0×10^{-23} J rad^{-2}	[33,34]

expressed as

$$W^R = \sum_{ij} \frac{k^R}{2}(|\mathbf{r}_{ij}| - r_0^R)^2, \qquad (2.8a)$$

$$\mathbf{f}_i^R = -\frac{\partial W^R}{\partial \mathbf{r}_i} = -k^R(|\mathbf{r}_{ij}| - r_0^R)\frac{\mathbf{r}_{ij}}{|\mathbf{r}_{ij}|} \qquad (2.8b)$$

and

$$\mathbf{f}_j^R = -\mathbf{f}_i^R. \qquad (2.8c)$$

where k^R ($=2 \times 10^{-4}$ N m^{-1}) is the repulsive resistance, and r_0^R ($=2a$) is the reference length. The effect of the repulsive force on the trajectories of fibres is very small, because it changes the distance between discrete nodes only when the nodes approach within the distance corresponding to the diameter of fibrinogen, which two order of magnitude smaller than system length. Indeed, the order of the magnitude of repulsive energy was two or three orders magnitude smaller than in the total energy (figures 3a and 6a). The linear repulsive model (equation 2.8) has been also applied to cellular interaction problem, and successfully represented a cellular flow in microchannels [38].

The protofibrils experience thermal fluctuations derived both from themselves and from solvent molecules. The random force at the ith node is described as

$$\mathbf{F}_i^{\text{rand}} = \sigma\mathbf{j} \qquad (2.9a)$$

and

$$\sigma^2 = 2ck_bT, \qquad (2.9b)$$

where σ is the magnitude of the random force, $\mathbf{j}$ is the random vector, k_b is the Boltzmann constant ($=1.38 \times 10^{-23}$ J K^{-1}) and T ($=300$ K) is the absolute temperature in the whole system. The temporal direction satisfies the following dynamic statistics:

$$\langle \mathbf{j} \rangle = 0 \qquad (2.10a)$$

and

$$\langle \mathbf{jj} \rangle = \mathbf{I}\delta(t - t'), \qquad (2.10b)$$

where $\langle \cdot \rangle$ represents random average procedures.

Ideally, model parameters characterizing each of the energy components in (2.2) should be determined from molecular dynamic simulations. However, this type of bottom-up approach based on energy trajectories (e.g. [39,40]) is still challenging due to the heavy computational load. In this study, we therefore proposed mesoscopic model properties to qualitatively represent the experimental observations [7,13,41], and in particular focused on the effect of the bending energy constant k^B and the aggregation energy constant k^A on fibrin clot formation. The parameter values are summarized in table 1.

2.2. Discretization

Following the study by Ermak & McCammon [44], the discrete form of equation (2.2) is rewritten as

$$c\dot{\mathbf{r}}_i = -\frac{\partial W}{\partial \mathbf{r}_i} + \frac{\sigma}{\sqrt{\Delta t}}\hat{\mathbf{j}}, \qquad (2.11)$$

where $\hat{\mathbf{j}}$ ($\in [0, 1]$) is the probability density function following equation (2.10). Based on a uniform random number between 0 and 1 that is given by the XORWOW method [45], we use the Box–Muller method to obtain the value of $\hat{\mathbf{j}}$ that satisfies the Gauss distribution [46]. The ith nodal point of the protofibril $\mathbf{r}_i^n$ at the n time step is updated by Lagrangian tracking, i.e.

$$\dot{\mathbf{r}}_i = \frac{\mathbf{r}_i^{n+1} - \mathbf{r}_i^n}{\Delta t}. \qquad (2.12)$$

The Euler method is used for time integration except for the stretch term in equation (2.2), which is solved by the explicit fourth-order Runge–Kutta method.

2.3. Numerical conditions and analysis

As an initial state, 1215 straight protofibrils (22 nodes/protofibril) are randomly placed in a cubic domain of size 3 μm × 3 μm × 3 μm. Periodic boundary conditions are imposed for all directions. The protofibrils aggregate with each other as time passes, and eventually attain a steady state where they fluctuate only as a result of thermal energy. All simulation cases reached this steady state condition by 50 ms or later (see also figure 3), and hence simulations were performed during a period of 200 ms. In addition, for each run we performed 10 replica simulations from a different initial fibre configuration to ensure that our simulation of the fibre network did not occur in a local energy minimum far from the global minimum. Although it is known that the physiological condition of human fibrinogen is 3–4.5 mg ml [47], some of experimental observations of fibrin
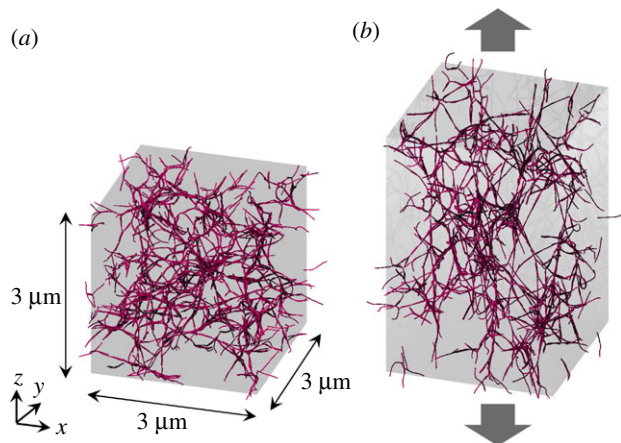
Figure 2. Computational domain consisting of a $3\,\mu m \times 3\,\mu m \times 3\,\mu m$ cube. A total of 1215 protofibrils (red rods) are randomly placed and orientated in the initial state. Periodic boundary conditions are imposed for all directions. (*a*) Snapshots of fibrin clot in the steady-state (200 ms after the initial state) and (*b*) fibrin clot extension in the *z*-direction. The results are obtained with $k^A = 2 \times 10^{-3}\,\mathrm{N\,m^{-1}}$ and $k^B = 1 \times 10^{-18}\,\mathrm{J\,rad^{-2}}$.

clots using scanning electron microscopy (SEM) were conducted in dilute fibrinogen concentrations such as $0.5\,\mathrm{mg\,ml^{-1}}$ [7,13]. For comparisons between calculated steady or extended fibrin clots with those in experimental observations in, e.g. [7,13,41], a fibrinogen concentration was set to $0.5\,\mathrm{mg\,ml^{-1}}$.

For steady-state fibrin clots, we also performed stretch testing. Stretching is expressed simply by the proportional scaling of coordinate *z* and the current computational box length L_z for the *z*-direction from current *z* to ξz and L_z to ξL_z [39,40] with:

$$\xi = 1 + \frac{c_s \Delta \tau}{L_z}, \tag{2.13}$$

where c_s (=2.5 mm s^{-1}) is the stretching speed in the *z*-direction, $\Delta \tau$ (=2 µs) is the relaxation time period. We tested 10 times slower stretching speed (i.e. $c_s = 0.25\,\mathrm{mm\,s^{-1}}$), and confirmed that the trajectory of the total energy state against the strain ε_z shown in figure 6*a* did not change. The nodal position for lateral directions (i.e. *x*- and *y*-directions) is not scaled during the extension. The extension is applied until the *z*-directional engineering strain $\varepsilon_z = L_z/L_z^0 - 1$ reaches 1.5, where L_z is the present length of the computational domain and L_z^0 is the initial computational length for the *z*-direction (=3 µm). Since we assume inertia-less protofibril dynamics represented as equation (2.1), and also ensure that fibrin clot dynamics have reached the equilibrium state during $\Delta \tau$, we can assume that the effect of stretch extension speed on the fibrin clot conformation is negligible. The engineering stress σ_z on the stretch direction (*z*-direction) is calculated from the energy state during fibre extension:

$$\sigma_z = \frac{F_z}{\mathcal{A}} = \frac{\partial W}{\partial L_z} \frac{1}{\mathcal{A}}, \tag{2.14}$$

where $\mathcal{A}$ (=$3 \times 3\,\mu m^2$) is the cross-sectional area (*x*–*y* plane) and F_z is the force. A representative snapshot of aggregated protofibrils in the steady state ($t = 200\,\mathrm{ms}$) and its stretched fibrin clot formation are shown in figure 2*a* and 2*b*, respectively. These results are obtained with $k^A = 2 \times 10^{-3}\,\mathrm{N\,m^{-1}}$ and $k^B = 1 \times 10^{-18}\,\mathrm{J\,rad^{-2}}$.

The orientations of individual protofibrils are defined as

$$\langle \theta \rangle = \frac{1}{N} \sum_i^N \langle \theta_i \rangle, \tag{2.15}$$

$$\langle \theta_i \rangle = \frac{\sum_{i,j} \theta_i^j l_i^j}{\sum_{i,j} l_i^j} \tag{2.16}$$

and

$$\theta_i^j = \arccos\left(\frac{\mathbf{e}_z \cdot \mathbf{l}_i^j}{l_i^j}\right), \tag{2.17}$$

where $\theta_i^j (\in [0, \pi/2])$ and $l_i^j (= |\mathbf{l}_i^j|)$ are the orientation angle and protofibril length of the *j*th segment ($j \in [1, 21]$) in the *i*th protofibril ($i \in [1, 1215]$), respectively, $\mathbf{e}_z$ is a unit vector along the *z*-direction in Euclidean space, $\langle \cdot \rangle$ denotes the ensemble average and *N* is the total number of protofibrils. Therefore, $\theta_i^j = 0$ indicates that the protofibril is oriented in the *z*-direction. The probability of the orientation of the *i*th protofibril $\langle \theta_i \rangle$ should be normalized by the small band area ΔS on the unit sphere, and can be defined as

$$\mathrm{Prob.}|_{\langle \theta_i \rangle \in [\Theta, \Theta + \Delta \Theta]}$$
$$= \frac{1}{N} \sum_i^N \frac{\mathrm{Count.}\{\langle \theta_i \rangle \mid [\Theta, \Theta + \Delta \Theta]\}}{\Delta S}$$
$$= \frac{1}{N} \sum_i^N \frac{\mathrm{Count.}\{\langle \theta_i \rangle \mid [\Theta, \Theta + \Delta \Theta]\}}{\int_\Theta^{\Theta + \Delta \Theta} 2\pi \sin \theta \, d\theta}. \tag{2.18}$$

For instance, the probability of aligned protofibrils with orientations of $\in [0, \pi/12]$ is defined as

$$\mathrm{Prob.}|_{\langle \theta_i \rangle \in [0, \pi/12]}$$
$$= \frac{1}{N} \sum_i^N \frac{\mathrm{Count.}\{\langle \theta_i \rangle | [0, \pi/12]\}}{1 - \cos(\pi/12)}. \tag{2.19}$$

3. Results

3.1. Aggregation of protofibrils

First, we investigated the spontaneously aggregated form of protofibrils (i.e. no external force) for different k^A and k^B. An example of the temporal history of each energy state is shown in figure 3*a*, which was obtained with $k^A = 2 \times 10^{-3}$ N m^{-1} and $k^B = 1 \times 10^{-18}$ J rad^{-2}. The energy state reached a plateau at a relatively early time period of approximately 50 ms. The results regarding fibre conformation, as quantified by the orientation angle, length and tortuosity of individual protofibrils, are shown in figure 3*b–d*, respectively. Here, the tortuosity (=$L/L_0 \geq 1$) is defined as the ratio between the length of protofibril *L* and the Euclidean distance from the start to the end points of protofibril L_0. If the fibre is oriented in the length direction, the tortuosity is $L/L_0 = 1$. These results showed that steady conformation has been reached within 50 ms, and the results are consistent with other cases. Hence, the time average is hereafter uniformly calculated over 100 ms after $t = 50\,\mathrm{ms}$ for all simulations to reduce the influence of the initial conditions.

For comparison with a SEM image [13] and calculated three-dimensional fibrin clots, we projected steady-state fibrin clots onto a two-dimensional plane (*x*–*y* plane at $z = 0$) with 10 nm pixel^{-1}. Here, we assigned 10 different luminosity values to the nodes within every 0.3-µm segment in the height *z*-direction, with higher luminosity associated with increased *z*-position. For these projected networks, we applied the Sobel filter to obtain the configuration of protofibrils from calculated nodal points, and also apply the Gaussian filter to obtain smoothed fibre structures. The stack images of steady fibrin clots for different k^A and k^B were obtained using the aforementioned process and are
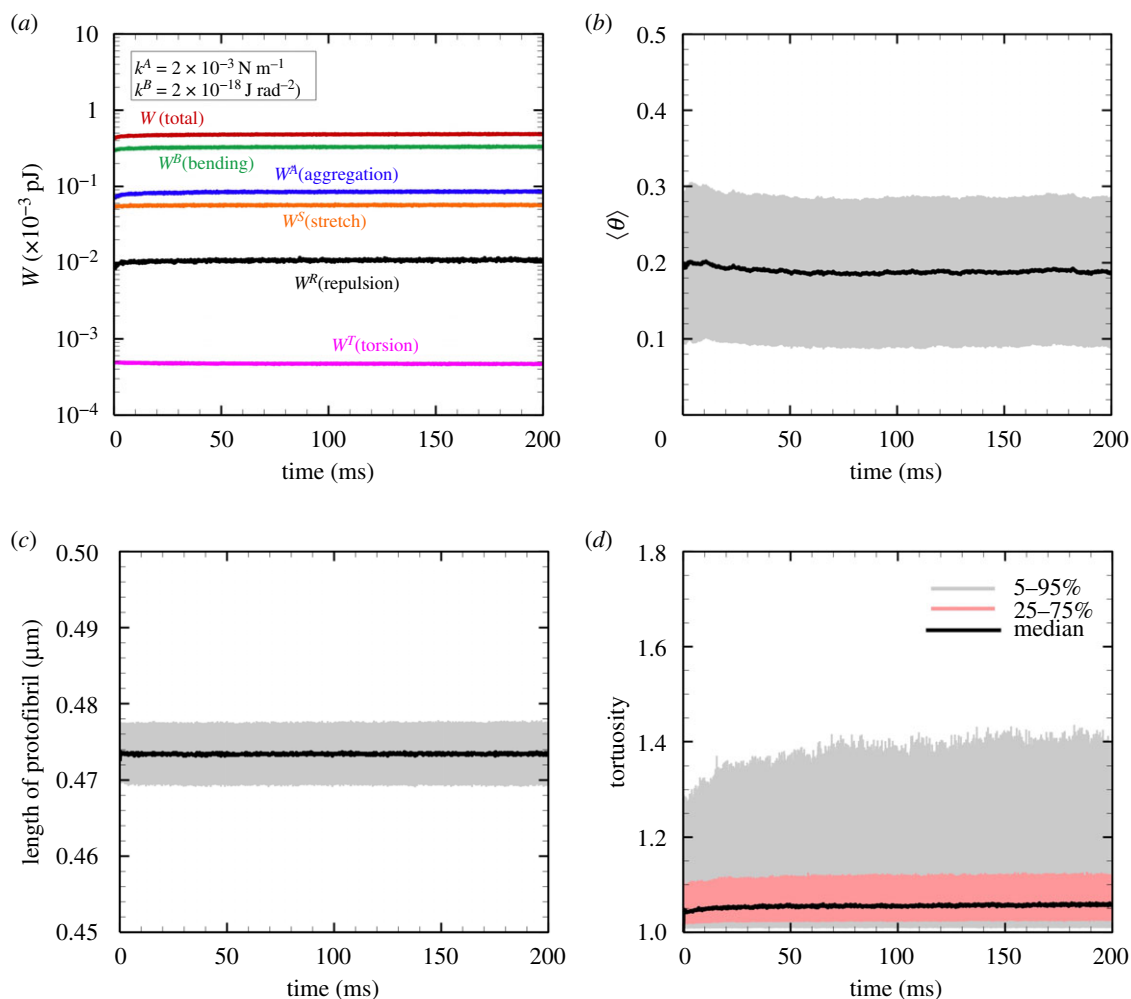
Figure 3. (a) One of the examples of the time history of each energy type; total energy $W = W^B + W^A + W^S + W^R + W^T$ (red), bending energy W^B (green), aggregation energy W^A (blue), stretch energy W^S (orange), repulsive energy W^R (black) and torsion energy W^T (pink). The time histories of the mean (b) protofibril orientation angle and (c) protofibril length, where the errors represent the standard deviation of individual protofibrils (=1215). (d) The time history of the median of the tortuosity, where the errors represent 5–95% percentile (light grey) and 25–75% percentile (red), respectively. The results were obtained with $k^B = 1 \times 10^{-18}\,\mathrm{J\,rad^{-2}}$ and $k^A = 2 \times 10^{-3}\,\mathrm{N\,m^{-1}}$.

shown in figure 4. Although there was no significant difference in fibre conformation for different k^A, the fibres tended to be straighter as k^B increased, a finding that is quantitatively shown in figure 5.

Protofibril conformation was quantified by the tortuosity of individual protofirbrils. The time average of the tortuosity is shown in figure 5, where error bars represent standard deviation of the run cases (M ± s.d., $\mathcal{N} = 10$). The results show that at each specific k^A, the tortuosity decreases (i.e. fibre linearity is enhanced) as k^B increases, which qualitatively agrees with previous experimental findings that fibre linearity was positively associated with individual protofibrils' bending resistance [13,17,22]. Experimental data of collagen-fibrin co-gels in phosphate-buffered saline (PBS) are also displayed [41], as quantified from SEM images. Here, in [41], 'fibres' are defined as multiple adjacent segments of protofibrils, and a 'segment' is the part of a fibre between cross-links. Especially at $k^A = 2 \times 10^{-3}\,\mathrm{N\,m^{-1}}$ and $k^B = 1 \times 10^{-18}\,\mathrm{J\,rad^{-2}}$, calculated tortuosity is highly consistent with the experimental result of a 'segment' in [41]. Since SEM requires dehydration, a stricter comparison may be needed to consider the effects of such an imaging process, but this is beyond the scope of the present work.
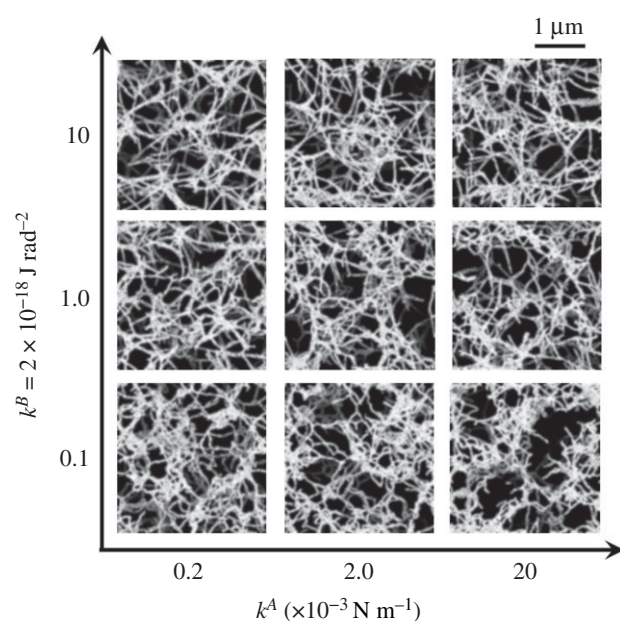

Figure 4. Representative snapshots of fibrin clots at the steady state for different k^A (=0.2, 2 and $20 \times 10^{-3}\,\mathrm{N\,m^{-1}}$) and k^B (=0.1, 1 and $10 \times 10^{-18}\,\mathrm{J\,rad^{-2}}$). The scale bar length is 1 µm.
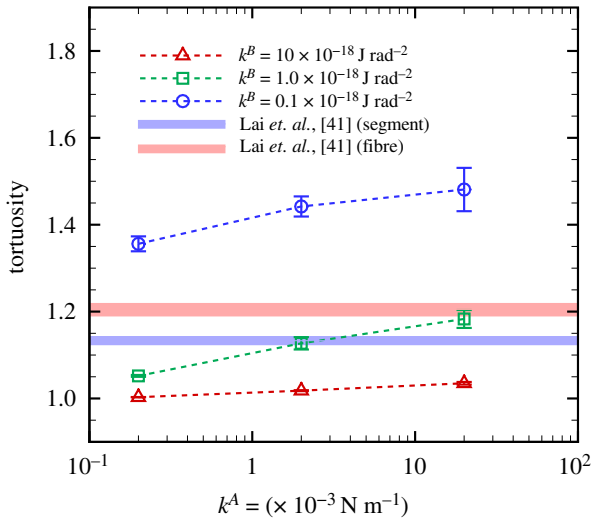
Figure 5. Time average of the tortuosity of individual protofibrils as a function of k^A for different k^B (M ± s.d., run cases $\mathcal{N}$ = 10). Experimental data [41] of tortuosity of segments and aggregated fibres in collagen-fibrin co-gels with PBS are also displayed.

3.2. Stretch tests of fibrin clots

Next, we performed stretch tests for the aforementioned fibrin clots under the same parameter ranges: $k^A = 0.2$–20×10^{-3} N m^{-1} and $k^B = 0.1$–10×10^{-18} J rad^{-2}. An example of the energy state for each engineering strain is shown in figure 6a. The result shown in figure 6a was obtained with $k^A = 2 \times 10^{-3}$ N m^{-1} and $k^B = 1 \times 10^{-18}$ J rad^{-2}. As the z-directional engineering strain ε_z increased, the stretch energy W^S gradually increased, and then finally overcame the aggregation energy W^A (figure 6a). This tendency was more obvious when k^A increased (data not shown). The decrease of the contribution of W^A to the total energy could be explained by the simple approximation of $W^A/(W^A + W^S) = 1/(1 + k^A/k^S)$ if the aggregated protofibrils were oriented to the z-direction.

Stretched fibres for different k^A and k^B are shown in figure 7, where protofibrils coloured red are extended beyond the fibre strain ε (=$l/l_0 - 1$) ≥ 0.05 (l and l_0 are the current length and the steady-state length of protofibril, respectively). The number of these extended fibres clearly increased when k^A increased from 0.2×10^{-3} to 2×10^{-3} N m^{-1} (figure 7). The structures of stretched protofibrils are quantified by the number of such protofibrils, the fibre orientation θ, and the probability (Prob.) of the orientation. The ratio of the stretched fibres with $\varepsilon \geq 0.05$ to the total number of protofibrils $n_{(\varepsilon \geq 0.05)}/N$ is shown in figure 6b. The percentage of fibres with $\varepsilon \geq 0.05$ was only 5% at $\varepsilon_z = 0.2$, but it increased to 20% at $\varepsilon_z = 0.5$. These fibres' orientations gradually decreased, i.e. the fibres became oriented to the stretch direction, as shown in figure 6c. Since the range of SD almost remains for ε_z, the result indicates that a distribution of fibre orientation angles exists even under extension. The probability of each orientation was therefore examined, and the results at $\varepsilon_z = 0$ and 0.5 are shown in figure 6d. At the steady state ($\varepsilon_z = 0$), the percentage of fibres oriented towards $\langle\theta\rangle \leq 45°$ was less than 50%, although it surpassed 60% at $\varepsilon_z = 0.5$ (figure 6d).

The population of effectively stretched and aggregated fibres was investigated, and the results are shown in figure 8. At the lowest k^A (=0.2×10^{-3} N m^{-1}), the ratio $n_{(\varepsilon \geq 0.05)}/N$ remained almost constant independent of k^B during extension (figure 8a). The aggregated fibres started

to dissociate for $\varepsilon_z \geq 0.1$ (figure 8a), and the dissociation rate was approximately 1%, i.e. $n_{agg}/n^0_{agg} \sim 0.99$ at $\varepsilon_z \geq 0.5$, where n_{agg} is the number of aggregated points, and n^0_{agg} is the number of initial aggregated points. For relatively large k^A ($\geq 2 \times 10^{-3}$ N m^{-1}), the ratio $n_{(\varepsilon \geq 0.05)}/N$ increased with k^B, and the fibres remained aggregated even at $\varepsilon_z = 0.5$, i.e. $n_{agg}/n^0_{agg} = 1$ (figure 8b,c). Furthermore, there was no marked difference in $n_{(\varepsilon \geq 0.05)}/N$ until $\varepsilon_z \leq 0.2$, independent of k^A (figure 8a–c). Note that, at the largest k^A (=20×10^{-3} N m^{-1}), only less than 1% fibres still aggregated even for $\varepsilon_z = 0.5$ (figure 8c).

Multiple examples of σ_z as a function of ε_z, obtained with $k^A = 2 \times 10^{-3}$ N m^{-1} and $k^B = 1 \times 10^{-18}$ J rad^{-2}, are shown in figure 9a. The moving-averaged data were obtained for the data of total energy W with a window size of $\varepsilon_z = 0.08$. We also evaluated different window sizes with a moving-average ($\varepsilon_z = 0.04$ and 0.16), and confirmed that there was almost no difference in results between obtained with $\varepsilon_z = 0.04$ and $\varepsilon_z = 0.08$. The values of σ_z shown in figure 9a indicate strain hardening, which qualitatively agrees with experimental data derived with fibrinogen concentrations of 0.5 and 1.0 mg ml^{-1} [7] when an isotropic network model was used. Note that for the lowest k^A, the clots showed strain softening for $\varepsilon_z \geq 0.2$ due to dissociation, as shown in figure 8a.

Especially for $\varepsilon_z < 0.2$, we confirmed an almost proportional relationship between σ_z and ε_z in all conditions that were investigated ($k^A = 0.2$–2×10^{-3} N m^{-1} and $k^B = 1 \times 10^{-18}$ J rad^{-2}), i.e. the effect of dissociation of aggregated fibres on σ_z was negligible. Thus, using the data of $\varepsilon_z = 0.05$ to 0.15, the elastic coefficient of fibrin clots E was calculated by least-squares fitting [48] to the plot of $\{\sigma_z - (E\varepsilon_z + \sigma_0)\}$, where σ_0 is the residual stress. The calculated E for different k^A and k^B is summarized in figure 9b. Although there was no marked difference in E at the smallest k^A (=0.2×10^{-3} N m^{-1}), E increased as k^A rose from 0.2×10^{-3} to 2×10^{-3} N m^{-1}, and the rate of its increase decreased thereafter. the error bars were relatively large, especially at the largest k^A (=20×10^{-3} N m^{-1}), representing variations of the energy state depending on the initial (quasi-steady) state. For each specific k^A, the value of E became large with k^B, which qualitatively agrees with the following conclusion based on experimental studies [13,17,22]: the bending resistance of individual protofibrils enhances not only fibre linearity but also the elasticity of fibrin clots.

Figure 9c shows the ratio $n_{(\varepsilon \geq 0.05)}/N$ at $\varepsilon_z = 0.2$ as a function of k^A, and indicates that the number of extended fibres with $\varepsilon_z \geq 0.05$ was insensitive to k^A. Figure 9d shows the probability of fibres oriented in the stretch direction, defined as those with $\langle\theta\rangle \in [0, \pi/12]$ (i.e. Prob. $|\langle\theta\rangle/\pi \in [0, 1/12])$ at $\varepsilon_z = 0.2$. These fibres continued to be oriented in this direction even though k^A increased, while the probability of this orientation increased with k^B, i.e. the fibrin clot structure was transformed to one that withstood extension as a result of increased k^B (figure 9d). Hence, the attenuation of the rate of increase in E with increasing k^A (figure 9b) may be correlated with the slow increase of effectively stretched fibres, which are defined with $\varepsilon \geq 0.05$ and $\langle\theta\rangle \in [0, \pi/12]$.

4. Discussion and conclusion

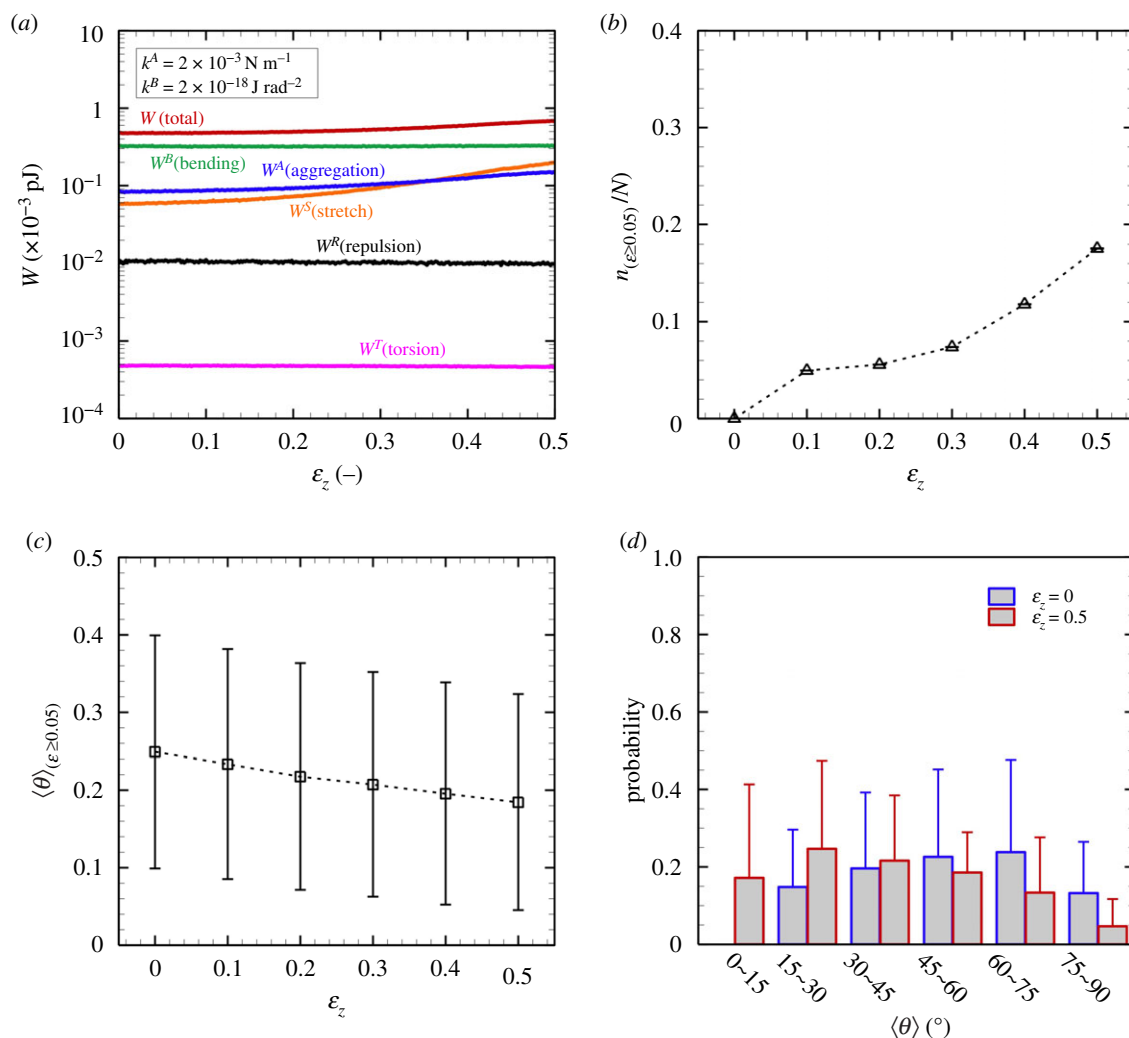Despite a number of studies of fibrin clots, much is still unknown about the relationship between the behaviour of

Figure 6. (*a*) Each averaged energy state (without the standard deviation of run cases), (*b*) the ratio of the stretched fibres with $\varepsilon \geq 0.05$ $n_{(\varepsilon \geq 0.05)}/N$, and (*c*) the ensemble average of the orientation angle of protofibrils with $\varepsilon \geq 0.05$ $\langle\theta\rangle_{(\varepsilon \geq 0.05)}$, as a function of the engineering strain ε_z. (*d*) Probability of the orientation angle of protofibrils at $\varepsilon_z = 0$ (blue) and $\varepsilon_z = 0.5$ (red). The results were obtained with $k^B = 1 \times 10^{-18}$ J rad^{-2} and $k^A = 2 \times 10^{-3}$ N m^{-1} (M ± SD, $\mathcal{N} = 10$).

individual protofibrils and the macro-scale mechanical response of fibrin clots. Yesudasan *et al.* proposed the coarse-grained molecular dynamics model, featuring several hundred nanometre-scale structures, to investigate a complex network of fibrin clots in terms of fibrinogen molecules [25,26]. However, there remain limitations to the mesoscopic mode focusing on the dynamics of fibrin clots, whose interactions can be characterized on a cellular scale (i.e. several micrometres). Stylianopoulos & Barocas developed a structural model that uses volume-averaging theory to study the mechanical behaviour of collagen networks [49], wherein the bending rigidity of individual fibres was neglected. Although their model successfully demonstrated the strain-hardening character of type I collagen extracellular matrices observed experimentally [50], other experimental studies using X-rays [51] or mechanical (shear strain) testing [52] suggested that the flexibility of fibrin clots may arise from bending of the fibres, a theory that was supported by later studies using electron microscopy [53] and optical tweezers [17]. Despite the insights about bending properties at the fibre level, the relationship between such mechanical properties on individual fibre conformations and the mechanical responses of clots are still unknown. To tackle these challenges, a mesoscopic framework based on protofibril

behaviours is necessary, but has not yet been established. We thus propose a minimal mesoscopic model for protofibrils based on Brownian dynamics. Through various numerical simulations, we evaluated the feasibility of our mesoscopic model analysis.

The approach used in our model successfully demonstrated conformation of a fibrin clot (figure 5) which was consistent with experimental data in [13,41]. Further, our numerical results captured the strain-hardening response, e.g. as reported in [7] based on protofibril dynamics (figure 9*a*). Although there are a number of experimental works about tensile mechanical properties in living materials [54] and also single-molecule biophysics [55], there are few reports about assessments of the stress acting on fibrin clots during extensions. For instance, Roeder *et al.* performed tensile mechanical tests for matrices purified from type I collagen for different collagen concentrations ranging between 0.3–3 mg ml^{-1}, and showed the strain-hardening character of the matrices [50]. The experimental estimation of the engineering stress obtained with 2 mg ml^{-1} collagen concentration was one or two orders of magnitude higher (i.e. $O(\sigma_z) = 10^2$–10^3 Pa) in the range between 10–20%-strain than our numerical results of fibrin clots with 0.5 mg ml^{-1} fibrinogen concentration [50].

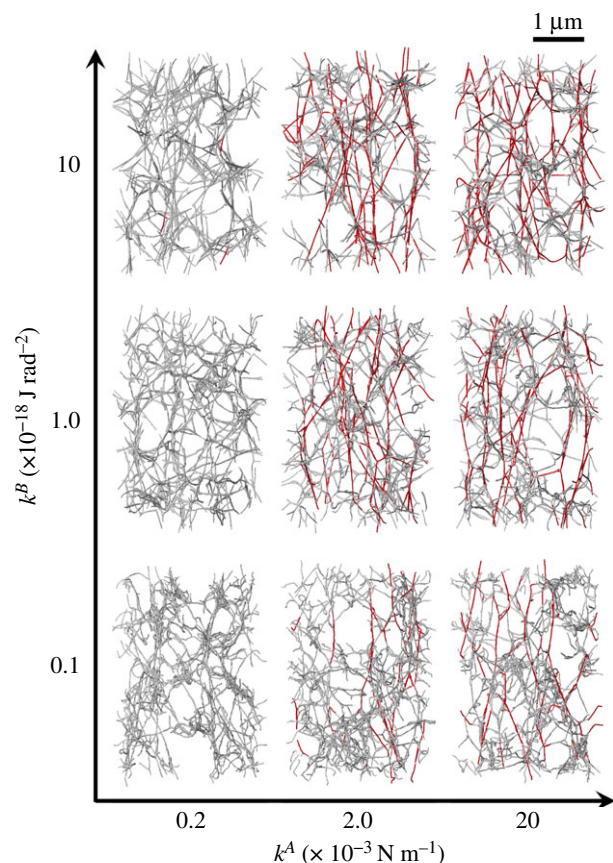**Figure 7.** Snapshots of extended fibrin clots at $\varepsilon_z = 0.5$ for different k^A and k^B. The scale bar length is 1 μm. Protofibrils coloured red are extended beyond the fibre strain ε ($=l/l_0 - 1$) ≥ 0.05: l and l_0 are the current length and at the steady-state length, respectively.

As with other numerical models, our mesoscopic model required a number of parameters. Although there are many SEM results regarding human fibrin clot structures (e.g. [16]), quantitative data of fibrin fibre parameters are still limited, and thus we could not determine them in a straightforward manner. Yesudasan *et al.* [25,26] used mathematical methods [56] to characterize and quantify 3D images of fibrin clot networks, and then compared them with simulation results [25]. Although our model parameters were not determined by this type of bottom-up molecular dynamic approach, our methodology potentially characterized the conformation of fibrin clots, as well as their mechanical responses, according to the model parameters. We thus suggest that our microscopic model can be used to estimate the relationship between the nanometre-scale dynamics of individual protofibrils and the mechanical properties of micrometre-scale fibrin clots. For example, simulations of aggregated protofibrils whose degree of extension depends on the aggregation energy constant k^A will provide insight into the dependency of factor XIIIa on fibrin clot elasticity [13,18,19]. Since our numerical results showed that the elasticity of the fibrin clots increased with k^A, the dependence of factor XIIIa on the elasticity resulting from the fibrous architecture of the clots may be characterized by k^A. Previous experimental results showed that stiffening of fibrin clots can result from the response of the polymeric protofibrils between cross-links, from alterations in the network structure, or both [6,7,14,15]. Although we did not fully quantify the architecture of aggregated protofibrils, the simulated

protofibrils in the networks also tended to align in the stretch direction as k^B increased (figure 9d), resulting in sparse networks (figure 7). Such interlinked protofibril structures may contribute to decreasing the elasticity of fibrin clots, especially at the highest k^A (=2.0 × 10^{-3} N m^{-1}) and k^B (=1.0 × 10^{-18} J rad^{-2}) (figure 9b). Future quantitative analysis of the network structure will provide insight into the relationship between the fibrous architecture and mechanical properties of the clot. Experimental observations using SEM have clarified the precise structure of fibrin clots, while some limitations should be carefully considered. SEM analysis allows us to visualize single fibres even under load [57], but originally hydrated fibrin networks are most often dehydrated and fixed, and hence it remains difficult to capture 3D networks of fibrin clots in dynamics. Spectroscopic tools such as Fourier transform infrared (FTIR) and Raman scattering offer alternative methods to probe structural changes of proteins using molecular vibrations. These methods can be performed on 3D fibrin hydrogels under mechanical deformation *in situ*. For instance, Litvinov *et al.* used FTIR spectroscopy to reveal force-induced changes in the secondary structure of hydrated fibrin clots made of human blood plasma *in vitro* [58]. In more recently, Wang *et al.* used broadband coherent anti-Stokes Raman scattering (BCARS) microscopy and custom-built loading devices to capture the molecular vibrational signature of fibrin under shear and tensile deformations *in situ* [59]. Along with those microscopic observation techniques, image analyses of a 3D network of fibrin clots obtained with confocal microscopy have been reported as well as its observation techniques [60,61]. The analyses have also gained insights into the mechanics of a fibrin network in terms of its microscopic structure [60,61].

Venous thromboembolism, including deep-vein thrombosis and pulmonary embolism, is the leading cause of lost disability-adjusted life years and the third leading cause of cardiovascular death in the world [62]. Potential risk analysis for thromboembolism is of fundamental importance in diagnosis or therapeutic decisions. Recent experimental observations showed that there are differences in structure and composition between arterial and venous thrombi and pulmonary emboli [63]. Therefore, the tensile mechanical properties of those thrombi characterized as volume fraction of fibrin fibres or fibrin bundles would be one of risks in thromboembolism. Since our numerical model enables the investigation of tensile stress as well as elastic coefficient for different fibrinogen concentrations, calculated elastic coefficients of fibrin clots with specific fibrinogen concentrations based on blood samples would provide additional bioengineering insights in the diagnosis of thromboembolism. While nonlinear mechanical properties of fibrin clots can be useful in bioengineering applications not only in wound repair but also drug delivery, cell delivery, cell differentiation, tissue engineering and patterning [59,64,65]. Our numerical model will gain insights into their designs, in terms of mechanical properties.

In *in vitro* experiments, clots are often obtained under conditions of purified fibrinogen or plasma with low platelet counts. However, in the actual human circulation, haemostatic clots or obstructive thrombi are formed in the presence of blood flow that profoundly affects the formation of the fibrin network and its structure and properties. For instance, it is known that the mechano-sensitive plasma protein von Willebrand factor (vWF) and its binding with
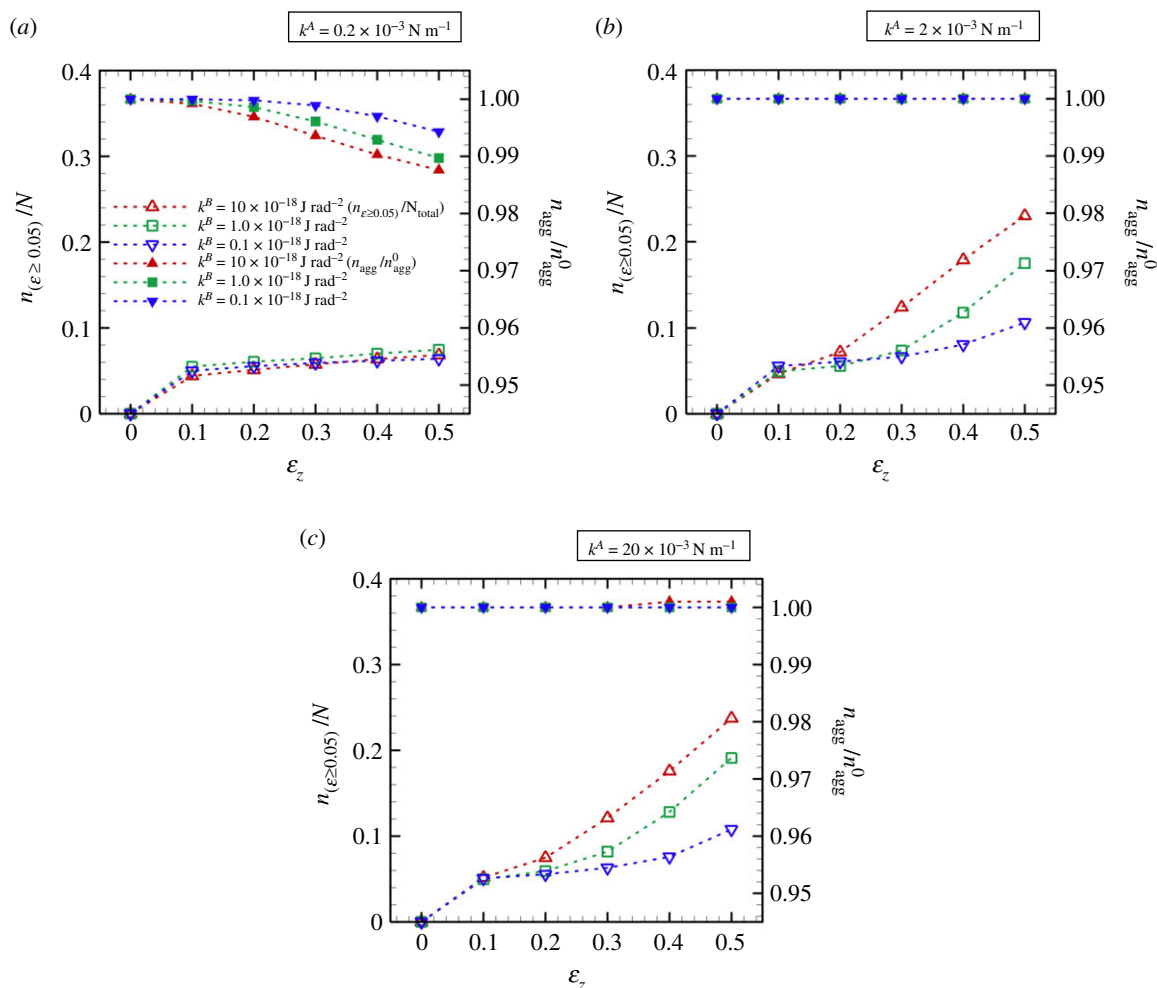
Figure 8. The ratio $n_{(\varepsilon \geq 0.05)}/N$, and the ratio of the number of aggregated points n_{agg} to the number of initial aggregated points n_{agg}^0 ($n_{\mathrm{agg}}/n_{\mathrm{agg}}^0$) as a function of ε_z for (a) $k^A = 0.2 \times 10^{-3}$ N m^{-1}, (b) $k^A = 2 \times 10^{-3}$ N m^{-1} and (c) $k^A = 20 \times 10^{-3}$ N m^{-1}, respectively (M $\pm$ s.d., $\mathcal{N} = 10$).

the platelet receptor glycoprotein Ibα (GPIbα) play a crucial role in haemostasis, yet is also key to pathological thrombus initiation and propagation, which are well reviewed in, e.g., [62,66]. Furthermore, the circulation continually brings more fibrinogen to the developing clot, and as a result it becomes denser, with thicker, bundled fibres [67]. Fluid flow can also cause the fibrin fibres to orient along the direction of flow both *in vitro* [68,69] and *in vivo* [70], which has important consequences for the mechanical properties of the clots [69,71]. Flow fields would also affect not only the structure of thrombi but also the composition. Recent clinical observation using high-resolution SEM clearly showed that venous thrombi are fibrin-rich, and arterial thrombi are fibrin- and platelet-rich [63]. The evidence that arterial thrombi contain a large amount of fibrin [63] is in contrast to previous animal experiments by [72,73], where high wall shear rates over the range 50–2500 s^{-1} impede fibrin deposition in subendothelium [72] and extracellular matrix [73]. Hence, further investigations about mechanical factors regulating thrombus growth are needed while paying attention to haemodynamic flow as well as mechanical reactions of plasma proteins. In our simulation, we did not consider the flow of background medium, and also neglected the presence of red cells/platelets and solvent proteins. Since there are only a few reports on the modelling of protein activation under cellular blood flow [74–76], it would be interesting to study how fibrous interactions affect the suspension rheology

of red blood cells (RBCs) [77] or the flow behaviours of RBCs and platelets in microvessels depending on shear rates [38,78].

In summary, we proposed a minimal mesoscopic model of protofibrils based on Brownian dynamics. Since our results successfully captured the conformation of aggregated protofibrils (e.g. tortuosity [41]) as well as their mechanical response (e.g. strain-hardening response [7]) depending on model parameters, we suggest that our microscopic model approach can estimate the relationship between nanometre-scale dynamics of individual protofibrils and the mechanical properties of micrometre-scale fibrin clots. For example, the dependence of specific mediators such as factor XIIIa on the network architecture, and thus on the elasticity of fibrin clots, can be estimated by modelling the aggregation or bending stiffness on the level of protofibril fibres. Our numerical results suggest that the aggregated protofibril structure was altered to withstand extension by increasing the bending stiffness of individual protofibrils, which is consistent with experimental results [13,17,22]. In the future, we will report the relationship between individual protofibril behaviours and the macro-scale mechanical response of fibrin clots, including the fibrous network structure.
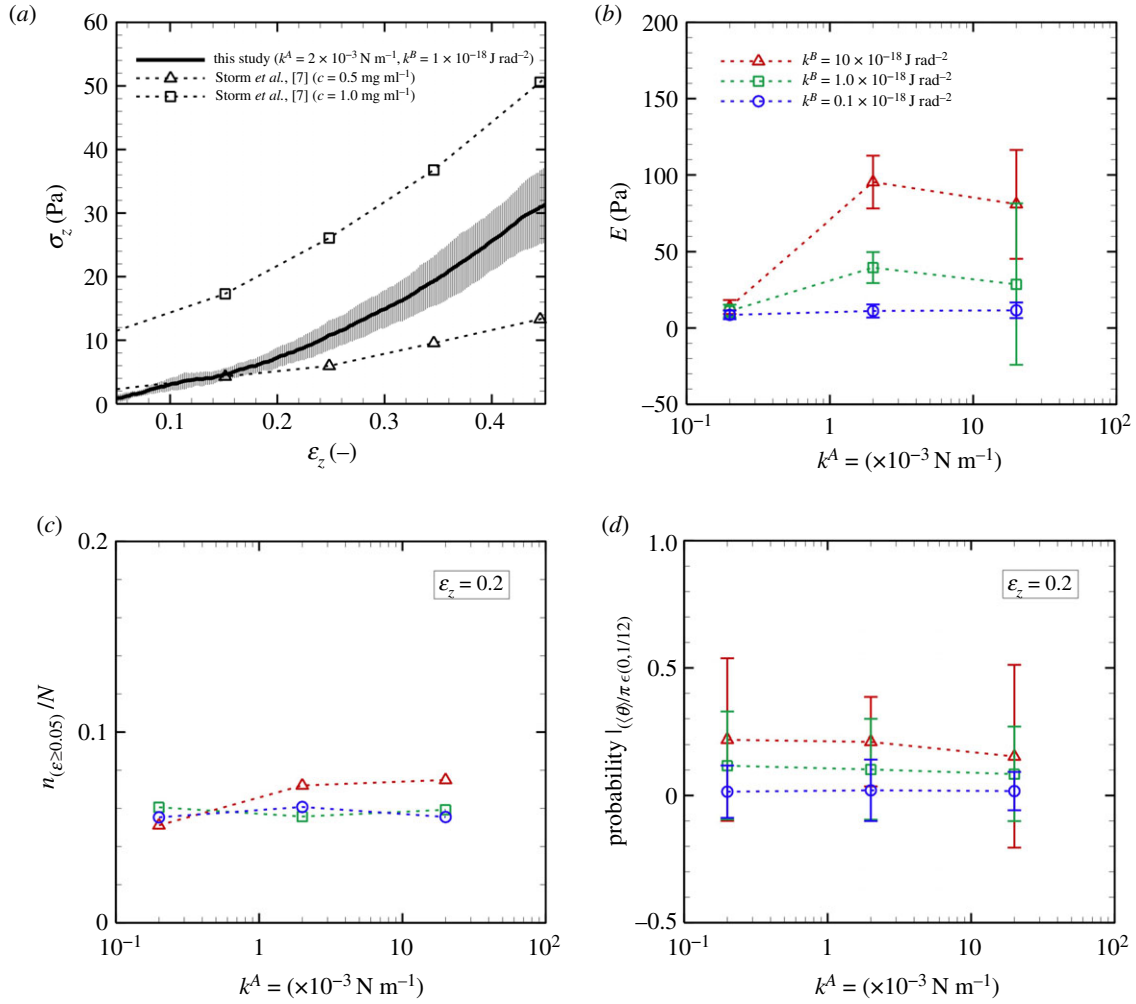
Figure 9. (a) Stress σ_z of the fibrin clot as a function of the strain ε_z. The result is obtained with $k^A = 2 \times 10^{-3}$ N m^{-1} and $k^B = 1 \times 10^{-18}$ J rad^{-2}. Experimental data of the shear modulus of fibrin clots (fibrinogen concentration of 0.5 and 1.0 mg ml^{-1}) [7] are also displayed. (b) Elastic coefficient E of fibrin clots as a function of k^A for different k^B. Using the data of $\varepsilon_z = 0.05$ to 0.15, E was calculated by least-squares fitting to the plot of $\{\sigma_z - (E\varepsilon_z + \sigma_0)\}$, where σ_0 is the residual stress. (c) Ratio $n_{(\varepsilon \geq 0.05)}/N$. (d) Probability with $\langle \theta \rangle \in [0, \pi/12]$ at $\varepsilon_z = 0.2$ as a function of k^A for different k^B (M $\pm$ s.d., $\mathcal{N} = 10$).

Appendix A

A.1. Bending energy

For equations (2.4c), we redefine the position vectors as

$$\mathbf{p} \equiv \mathbf{r}_j, \tag{A 1a}$$
$$\mathbf{q} \equiv \mathbf{r}_i \tag{A 1b}$$

and

$$\mathbf{r} \equiv \mathbf{r}_k, \tag{A 1c}$$

and also

$$\mathbf{a} \equiv \mathbf{r}_{ij} = \mathbf{r}_j - \mathbf{r}_i = \mathbf{p} - \mathbf{q} \tag{A 2a}$$

and

$$\mathbf{b} \equiv \mathbf{r}_{ik} = \mathbf{r}_k - \mathbf{r}_i = \mathbf{r} - \mathbf{q}. \tag{A 2b}$$

Then, the bending energy can be expressed as

$$W^B = \sum_{e \in \mathcal{D}^B} \Delta W_e^B, \tag{A 3a}$$

$$\Delta W_e^B = \frac{k^B}{2}(\phi_e - \phi_0)^2 \tag{A 3b}$$

and

$$\phi_e = \arccos\left(\frac{\mathbf{a} \cdot \mathbf{b}}{|\mathbf{a}||\mathbf{b}|}\right), \tag{A 3c}$$

where $\mathcal{D}^B$ is the total set of indices for bending elements. The nodal force $\mathbf{f}_i^B$ ($i \in [1, N]$; N is the number of nodal points) is calculated by

$$\mathbf{f}_i^B = -\frac{\partial W^B}{\partial \mathbf{r}_i} = \sum_{e \in \mathcal{D}_i^B} \Delta \mathbf{f}_e^B \tag{A 4a}$$

and

$$\Delta \mathbf{f}_e^B = -\frac{\partial \Delta W_e^B}{\partial \phi_e} \frac{\partial \phi_e}{\partial \mathbf{r}_i}, \tag{A 4b}$$

where $\partial\mathcal{D}_i^B$ is the subset of $\mathcal{D}^B$ involving the nodal point $\mathbf{r}_i$. Focusing on the formulation of a bending element e, we calculate as

$$\frac{\partial\Delta W^B}{\partial\phi} = k^B(\phi_e - \phi_0). \tag{A 5}$$

and

$$\frac{\partial\phi}{\partial\mathbf{p}} = \frac{\partial\mathbf{a}}{\partial\mathbf{p}}\cdot\frac{\partial\phi}{\partial\mathbf{a}} + \frac{\partial\mathbf{b}}{\partial\mathbf{p}}\cdot\frac{\partial\phi}{\partial\mathbf{b}} = \frac{\partial\phi}{\partial\mathbf{a}}, \tag{A 6a}$$

$$\frac{\partial\phi}{\partial\mathbf{q}} = \frac{\partial\mathbf{a}}{\partial\mathbf{q}}\cdot\frac{\partial\phi}{\partial\mathbf{a}} + \frac{\partial\mathbf{b}}{\partial\mathbf{q}}\cdot\frac{\partial\phi}{\partial\mathbf{b}} = -\frac{\partial\phi}{\partial\mathbf{a}} - \frac{\partial\phi}{\partial\mathbf{b}} \tag{A 6b}$$

and

$$\frac{\partial\phi}{\partial\mathbf{r}} = \frac{\partial\mathbf{a}}{\partial\mathbf{r}}\cdot\frac{\partial\phi}{\partial\mathbf{a}} + \frac{\partial\mathbf{b}}{\partial\mathbf{r}}\cdot\frac{\partial\phi}{\partial\mathbf{b}} = \frac{\partial\phi}{\partial\mathbf{b}}. \tag{A 6c}$$

Introducing $\Theta = \mathbf{a}\cdot\mathbf{b}/|\mathbf{a}||\mathbf{b}| = \cos\theta$, we obtain

$$\begin{aligned}\frac{\partial\phi}{\partial\mathbf{a}} &= \frac{\partial\arccos\Theta}{\partial\Theta}\frac{\partial\Theta}{\partial\mathbf{a}} \\ &= \frac{-1}{\sqrt{1-\Theta^2}}\frac{\partial}{\partial\mathbf{a}}\left(\frac{\mathbf{a}}{|\mathbf{a}|}\right)\cdot\frac{\mathbf{b}}{|\mathbf{b}|} \\ &= -\frac{1}{\sqrt{1-\Theta^2}}\left(\frac{1}{|\mathbf{a}|}\mathbf{I} - \frac{\mathbf{a}}{|\mathbf{a}|^3}\mathbf{a}\right)\cdot\frac{\mathbf{b}}{|\mathbf{b}|} \\ &= -\frac{1}{\sqrt{1-\Theta^2}}\frac{1}{|\mathbf{a}|}\left(\frac{\mathbf{b}}{|\mathbf{b}|} - \frac{\mathbf{a}}{|\mathbf{a}|}\frac{\mathbf{a}\cdot\mathbf{b}}{|\mathbf{a}||\mathbf{b}|}\right) \\ &= -\frac{1}{\sin\theta}\frac{1}{|\mathbf{a}|}\left(\frac{\mathbf{b}}{|\mathbf{b}|} - \frac{\mathbf{a}}{|\mathbf{a}|}\cos\theta\right),\end{aligned} \tag{A 7}$$

and analogously

$$\frac{\partial\phi}{\partial\mathbf{b}} = -\frac{1}{\sin\theta}\frac{1}{|\mathbf{b}|}\left(\frac{\mathbf{a}}{|\mathbf{a}|} - \frac{\mathbf{b}}{|\mathbf{b}|}\cos\theta\right). \tag{A 8}$$

Consequently, the nodal forces in a bending element e are given by

$$\Delta\mathbf{f}_p^B = -k^B(\phi_e - \phi_0)\frac{\partial\phi_e}{\partial\mathbf{a}}, \tag{A 9}$$

$$\Delta\mathbf{f}_q^B = k^B(\phi_e - \phi_0)\left(\frac{\partial\phi_e}{\partial\mathbf{a}} + \frac{\partial\phi}{\partial\mathbf{b}}\right) \tag{A 10}$$

and

$$\Delta\mathbf{f}_r^B = -k^B(\phi_e - \phi_0)\frac{\partial\phi_e}{\partial\mathbf{b}}. \tag{A 11}$$

A.2. Torsion energy

For equation (2.5c), we redefine the position vectors as

$$\mathbf{p} \equiv \mathbf{r}_j, \tag{A 12a}$$

$$\mathbf{q} \equiv \mathbf{r}_i, \tag{A 12b}$$

$$\mathbf{r} \equiv \mathbf{r}_k \tag{A 12c}$$

and

$$\mathbf{s} \equiv \mathbf{r}_l. \tag{A 12d}$$

and

$$\mathbf{a} \equiv \mathbf{r}_{ij} = \mathbf{r}_j - \mathbf{r}_i = \mathbf{p} - \mathbf{q}, \tag{A 13a}$$

$$\mathbf{b} \equiv \mathbf{r}_{ik} = \mathbf{r}_k - \mathbf{r}_i = \mathbf{r} - \mathbf{q}, \tag{A 13b}$$

$$\mathbf{c} \equiv \mathbf{r}_{ki} = \mathbf{r}_i - \mathbf{r}_k = \mathbf{q} - \mathbf{r} = -\mathbf{b} \tag{A 13c}$$

and

$$\mathbf{d} \equiv \mathbf{r}_{kl} = \mathbf{r}_l - \mathbf{r}_k = \mathbf{s} - \mathbf{r}. \tag{A 13d}$$

Then, we rewrite equation (2.6) as

$$\mathbf{m} = \mathbf{a}\times\mathbf{b} \tag{A 14a}$$

and

$$\mathbf{n} = \mathbf{c}\times\mathbf{d}. \tag{A 14b}$$

The torsion energy W^T is given by

$$W^T = \sum_{e\in\mathcal{D}^T}\Delta W_e^T, \tag{A 15a}$$

$$\Delta W_e^T = \frac{k^T}{2}(\phi_e - \phi_0)^2 \tag{A 15b}$$

and

$$\phi_e = \arccos\left(\frac{\mathbf{m}\cdot\mathbf{n}}{|\mathbf{m}||\mathbf{n}|}\right), \tag{A 15c}$$

where $\mathcal{D}^T$ is the total set of indices for torsional elements. The nodal force $\mathbf{f}_i^T$ $(i\in[1, N])$ is calculated by

$$\mathbf{f}_i^T = -\frac{\partial W^T}{\partial\mathbf{r}_i} = \sum_{e\in\partial\mathcal{D}_i^T}\Delta\mathbf{f}_e^T \tag{A 16a}$$

and

$$\Delta\mathbf{f}_e^T = -\frac{\partial\Delta W_e^T}{\partial\phi_e}\frac{\partial\phi_e}{\partial\mathbf{r}_i}, \tag{A 16b}$$

where $\partial\mathcal{D}_i^T$ is the subset of $\mathcal{D}^T$ involving the nodal point $\mathbf{r}_i$. Focusing on the formulation of a torsional element e, we calculate as

$$\frac{\partial\Delta W_e^T}{\partial\phi} = k^T(\phi_e - \phi_0) \tag{A 17}$$

and

$$\frac{\partial\phi}{\partial\alpha} = \frac{\partial\mathbf{m}}{\partial\alpha}\cdot\frac{\partial\phi}{\partial\mathbf{m}} + \frac{\partial\mathbf{n}}{\partial\alpha}\cdot\frac{\partial\phi}{\partial\mathbf{n}}, \quad (\alpha = \mathbf{p}, \mathbf{q}, \mathbf{r}, \mathbf{s}). \tag{A 18}$$

Introducing $\Theta = \mathbf{m}\cdot\mathbf{n}/|\mathbf{m}||\mathbf{n}| = \cos\theta$, and referring to equations (A7) and (A8), we obtain

$$\frac{\partial\phi}{\partial\mathbf{m}} = -\frac{1}{\sin\theta}\frac{1}{|\mathbf{m}|}\left(\frac{\mathbf{n}}{|\mathbf{n}|} - \frac{\mathbf{m}}{|\mathbf{m}|}\cos\theta\right) \tag{A 19a}$$

and

$$\frac{\partial\phi}{\partial\mathbf{n}} = -\frac{1}{\sin\theta}\frac{1}{|\mathbf{n}|}\left(\frac{\mathbf{m}}{|\mathbf{m}|} - \frac{\mathbf{n}}{|\mathbf{n}|}\cos\theta\right). \tag{A 19b}$$

We derive the index notation with the summation convention

$$\begin{aligned}\frac{\partial\mathbf{m}}{\partial\alpha} &= \frac{\partial((\mathbf{p} - \mathbf{q})\times(\mathbf{r} - \mathbf{q}))}{\partial\alpha} \\ \Rightarrow \frac{\partial m_j}{\partial\alpha_i} &= \varepsilon_{jkl}\frac{\partial((p_k - q_k)(r_l - q_l))}{\partial\alpha_i}\end{aligned} \tag{A 20a}$$

and

$$\begin{aligned}\frac{\partial\mathbf{n}}{\partial\alpha} &= \frac{\partial((\mathbf{q} - \mathbf{r})\times(\mathbf{s} - \mathbf{r}))}{\partial\alpha} \\ \Rightarrow \frac{\partial n_j}{\partial\alpha_i} &= \varepsilon_{jkl}\frac{\partial((q_k - r_k)(s_l - r_l))}{\partial\alpha_i},\end{aligned} \tag{A 20b}$$

$$(\alpha = p, q, r, s),$$

where

$$
\begin{aligned}
\frac{\partial m_j}{\partial p_i} &= \varepsilon_{jkl} \frac{\partial((p_k - q_k)(r_l - q_l))}{\partial p_i} \\
&= \varepsilon_{jkl} \delta_{ik}(r_l - q_l) = \varepsilon_{jik}(r_k - q_k), \\
\frac{\partial m_j}{\partial p_i} &= \varepsilon_{jkl} \frac{\partial((q_k - r_k)(s_l - r_l))}{\partial p_i} \\
&= 0,
\end{aligned}
\quad\quad \text{(A 21a)}
$$

$$
\begin{aligned}
\frac{\partial m_j}{\partial q_i} &= \varepsilon_{jkl} \frac{\partial((p_k - q_k)(r_l - q_l))}{\partial q_i} \\
&= -\varepsilon_{ijk}(p_k - q_k) - \varepsilon_{jik}(r_k - q_k), \\
\frac{\partial n_j}{\partial q_i} &= \varepsilon_{jkl} \frac{\partial((q_k - r_k)(s_l - r_l))}{\partial q_i} \\
&= \varepsilon_{jik}(s_k - r_k),
\end{aligned}
\quad\quad \text{(A 21b)}
$$

$$
\begin{aligned}
\frac{\partial m_j}{\partial r_i} &= \varepsilon_{jkl} \frac{\partial((p_k - q_k)(r_l - q_l))}{\partial r_i} \\
&= \varepsilon_{ijk}(p_k - q_k), \\
\frac{\partial m_j}{\partial r_i} &= \varepsilon_{jkl} \frac{\partial((q_k - r_k)(s_l - r_l))}{\partial r_i} \\
&= -\varepsilon_{ijk}(q_k - r_k) - \varepsilon_{jik}(s_k - r_k),
\end{aligned}
\quad\quad \text{(A 21c)}
$$

and

$$
\begin{aligned}
\frac{\partial m_j}{\partial s_i} &= \varepsilon_{jkl} \frac{\partial((p_k - q_k)(r_l - q_l))}{\partial s_i} \\
&= 0, \\
\frac{\partial m_j}{\partial s_i} &= \varepsilon_{jkl} \frac{\partial((q_k - r_k)(s_l - r_l))}{\partial s_i} \\
&= \varepsilon_{ijk}(q_k - r_k),
\end{aligned}
\quad\quad \text{(A 21d)}
$$

Thus,

$$
\begin{aligned}
\frac{\partial \mathbf{m}}{\partial \alpha} \cdot \beta &= \frac{\partial m_j}{\partial \alpha_i} \beta_j \mathbf{e}_j \\
&= \begin{cases}
\mathbf{b} \times \beta, & (\alpha = p) \\
-\beta \times \mathbf{a} - \mathbf{b} \times \beta = \beta \times (\mathbf{b} - \mathbf{a}), & (\alpha = q) \\
\beta \times \mathbf{a}, & (\alpha = r) \\
0, & (\alpha = s)
\end{cases}
\end{aligned}
\quad \text{(A 22a)}
$$

and

$$
\begin{aligned}
\frac{\partial \mathbf{n}}{\partial \alpha} \cdot \beta &= \frac{\partial n_j}{\partial \alpha_i} \beta_j \mathbf{e}_j \\
&= \begin{cases}
0, & (\alpha = p) \\
\mathbf{d} \times \beta, & (\alpha = q) \\
-\beta \times \mathbf{c} - \mathbf{d} \times \beta = -\beta \times (\mathbf{c} - \mathbf{d}), & (\alpha = r) \\
\beta \times \mathbf{c}, & (\alpha = s)
\end{cases}
\end{aligned}
\quad \text{(A 22b)}
$$

for the arbitrary vector β. Consequently, the nodal forces in a torsional element e are given by

$$
\begin{aligned}
\Delta \mathbf{f}_p^T &= -\frac{\Delta W^T}{\partial \phi} \left(\frac{\partial \mathbf{m}}{\partial \mathbf{p}} \cdot \frac{\partial \phi}{\partial \mathbf{m}} + \frac{\partial \mathbf{n}}{\partial \mathbf{p}} \cdot \frac{\partial \phi}{\partial \mathbf{n}} \right) \\
&= k^T(\phi - \phi_0) \left(\frac{\partial \phi}{\partial \mathbf{m}} \times \mathbf{b} \right),
\end{aligned}
\quad \text{(A 23a)}
$$

$$
\begin{aligned}
\Delta \mathbf{f}_q^T &= -\frac{\Delta W^T}{\partial \phi} \left(\frac{\partial \mathbf{m}}{\partial \mathbf{q}} \cdot \frac{\partial \phi}{\partial \mathbf{m}} + \frac{\partial \mathbf{n}}{\partial \mathbf{q}} \cdot \frac{\partial \phi}{\partial \mathbf{n}} \right) \\
&= -k^T(\phi - \phi_0) \left(\frac{\partial \phi}{\partial \mathbf{m}} \times (\mathbf{b} - \mathbf{a}) - \frac{\partial \phi}{\partial \mathbf{n}} \times \mathbf{d} \right),
\end{aligned}
\quad \text{(A 23b)}
$$

$$
\begin{aligned}
\Delta \mathbf{f}_r^T &= -\frac{\Delta W^T}{\partial \phi} \left(\frac{\partial \mathbf{m}}{\partial \mathbf{r}} \cdot \frac{\partial \phi}{\partial \mathbf{m}} + \frac{\partial \mathbf{n}}{\partial \mathbf{r}} \cdot \frac{\partial \phi}{\partial \mathbf{n}} \right) \\
&= -k^T(\phi - \phi_0) \left(\frac{\partial \phi}{\partial \mathbf{m}} \times \mathbf{a} - \frac{\partial \phi}{\partial \mathbf{n}} \times (\mathbf{c} - \mathbf{d}) \right)
\end{aligned}
\quad \text{(A 23c)}
$$

and

$$
\begin{aligned}
\Delta \mathbf{f}_s^T &= -\frac{\Delta W^T}{\partial \phi} \left(\frac{\partial \mathbf{m}}{\partial \mathbf{s}} \cdot \frac{\partial \phi}{\partial \mathbf{m}} + \frac{\partial \mathbf{n}}{\partial \mathbf{s}} \cdot \frac{\partial \phi}{\partial \mathbf{n}} \right) \\
&= -k^T(\phi - \phi_0) \left(\frac{\partial \phi}{\partial \mathbf{n}} \times \mathbf{c} \right).
\end{aligned}
\quad \text{(A 23d)}
$$

Note that in practical application, we take

$$
\phi = \mathrm{sgn}(\mathbf{b} \cdot (\mathbf{m} \times \mathbf{n})) \arccos\left(\frac{\mathbf{m} \cdot \mathbf{n}}{|\mathbf{m}\|\mathbf{n}|} \right).
\quad \text{(A 24)}
$$

References

1. Weisel JW, Litvinov RI. 2013 Mechanisms of fibrin polymerization and clinical implications. *Blood* **121**, 1712–1719. (doi:10.1182/blood-2012-09-306639)

2. Heit JA. 2015 Epidemiology of venous thromboembolism. *Nat. Rev. Cardiol.* **12**, 464–474. (doi:10.1038/nrcardio.2015.83)

3. Kattula S, Byrnes JR, Wolberg AS. 2017 Fibrinogen and fibrin in hemostasis and thrombosis. *Arterioscler. Thromb. Vasc. Biol.* **37**, e13–e21. (doi:10.1161/ATVBAHA.117.308564)

4. Brown AEX, Litvinov RI, Discher DE, Purohit PK, Weisel JW. 2009 Multiscale mechanics of fibrin polymer: gel stretching with protein unfolding and loss of water. *Science* **325**, 741–744. (doi:10.1126/science.1172484)

5. Hansen CE, Qiu Y, McCarty OJT, Lam WA. 2018 Platelet mechanotransduction. *Annu. Rev. Biomed.*

Eng. **20**, 253–275. (doi:10.1146/annurev-bioeng-062117-121215)

6. Lam WA, Chaudhuri O, Crow A, Webster KD, Li T-D, Kita A, Huang J, Fletcher DA. 2011 Mechanics and contraction dynamics of single platelets and implications for clot stiffening. *Nat. Mater.* **10**, 61–66. (doi:10.1038/NMAT2903)

7. Storm C, Pastore JJ, MacKintosh FC, Lubensky TC, Janmey PA. 2005 Nonlinear elasticity in biological gels. *Nature* **435**, 191–194. (doi:10.1038/nature03521)

8. Chernysh IN, Weise JW. 2008 Dynamic imaging of fibrin network formation correlated with other measures of polymerization. *Blood* **111**, 4854–4861. (doi:10.1182/blood-2007-08-105247)

9. Chernysh IN, Nagaswami C, Weisel JW. 2011 Visualization and identification of the structures

formed during early stages of fibrin polymerization. *Blood* **117**, 4609–4614. (doi:10.1182/blood-2010-07-297671)

10. Zhmurov A, Protopopova AD, Litvinov RI, Zhukov P, Weisel JW, Barsegov V. 2018 Atomic structural models of fibrin oligomers. *Structure* **26**, 857–868. (doi:10.1016/j.str.2018.04.005)

11. Weisel JW, Medved L. 2001 The structure and function of the alpha C domains of fibrinogen. *Ann. NY Acad. Sci.* **936**, 312–327. (doi:10.1111/j.1749-6632.2001.tb03517.x)

12. Yermolenko IS, Lishko VK, Ugarova TP, Magonov SN. 2011 High-resolution visualization of fibrinogen molecules and fibrin fibers with atomic force microscopy. *Biomacromolecules* **12**, 370–379. (doi:10.1021/bm101122g)

13. Ryan EA, Mockros LF, Weisel JW, Lorand L. 1999 Structural origins of fibrin clot rheology. *Biophys. J.* **77**, 2813–2826. (doi:10.1016/S0006-3495(99)77113-4)

14. Weisel JW, Nagaswami C. 1992 Computer modeling of fibrin polymerization kinetics correlated with electron microscope and turbidity observations: clot structure and assembly are kinetically controlled. *Biophys. J.* **63**, 111–128. (doi:10.1016/S0006-3495(92)81594-1)

15. Chen Z et al. 2019 Microclot array elastometry for integrated measurement of thrombus formation and clot biomechanics under fluid shear. *Nat. Commun.* **10**, 2051. (doi:10.1038/s41467-019-10067-6)

16. Badiei N et al. 2015 Effects of unidirectional flow shear stresses on the formation, fractal microstructure and rigidity of incipient whole blood clots and fibrin gels. *Clin. Hemorheol. Microcirc.* **60**, 451–464. (doi:10.3233/CH-151924)

17. Collet JP, Shuman H, Ledger RE, Lee S, Weisel JW. 2005 The elasticity of an individual fibrin fiber in a clot. *Proc. Natl Acad. Sci. USA* **102**, 9133–9137. (doi:10.1073/pnas.0504120102)

18. Greenberg CS, Dobson JV, Miraglia CC. 1985 Regulation of plasma factor XIII binding to fibrin in vitro. *Blood* **66**, 1028–1034. (doi:10.1182/blood.V66.5.1028.1028)

19. Weisel JW. 2004 The mechanical properties of fibrin for basic scientists and clinicians. *Biophys. Chem.* **112**, 267–276. (doi:10.1016/j.bpc.2004.07.029)

20. He S, Bark N, Wang H, Svensson J, Blombäck M. 2009 Effects of acetylsalicylic acid on increase of fibrin network porosity and the consequent upregulation of fibrinolysis. *J. Cardiovasc. Pharmacol.* **53**, 24–29. (doi:10.1097/FJC.0b013e3181953e0f)

21. Yeromonahos C, Marlu R, Polack B, Francois C. 2012 Antithrombin-independent effects of heparins on fibrin clot nanostructure. *Arterioscler. Thromb. Vasc. Biol.* **32**, 1320–1324. (doi:10.1161/ATVBAHA.112.245308)

22. Piechocka IK, Kurniawan NA, Grimbergen J, Koopman J, Koenderink GH. 2017 Recombinant fibrinogen reveals the differential roles of α- and γ-chain cross-linking and molecular heterogeneity in fibrin clot strain-stiffening. *J. Thromb. Haemost.* **15**, 938–949. (doi:10.1111/jth.13650)

23. Onck PR, Koeman T, van Dillen T, van der Giessen E. 2005 Alternative explanation of stiffening in cross-linked semiflexible networks. *Phys. Rev. Lett.* **95**, 178102. (doi:10.1103/PhysRevLett.95.178102)

24. Moiseyev G, Givli S, Bar-Yoseph PZ. 2013 Fibrin polymerization in blood coagulation: a statistical model. *J. Biomech.* **46**, 26–30. (doi:10.1016/j.jbiomech.2012.09.019)

25. Yesudasan S, Wang X, Averett RD. 2018 Coarse-grained molecular dynamics simulations of fibrin polymerization: effects of thrombin concentration on fibrin clot structure. *J. Mol. Model.* **24**, 109. (doi:10.1007/s00894-018-3642-7)

26. Yesudasan S, Wang X, Averett RD. 2018 Fibrin polymerization simulation using a reactive dissipative particle dynamics method. *Biomech.*

Model. Mechanobiol. **17**, 1389–1403. (doi:10.1007/s10237-018-1033-8)

27. Mosesson MW, Siebenlist KR, Hainfeld Jf, Wall JS, Soria J, Soria C, Caen JP. 1996 The relationship between the fibrinogen D domain self-association/cross-linking site (gammaXL) and the fibrinogen Dusart abnormality (Aalpha R554C-albumin): clues to thrombophilia in the 'Dusart syndrome'. *J. Clin. Invest.* **97**, 2342–2350. (doi:10.1172/JCI118677)

28. Hall CE, Slayter HS. 1959 The fibrinogen molecule: its size, shape, and mode of polymerization. *J. Biophys. Biochem. Cytol.* **5**, 11–27. (doi:10.1083/jcb.5.1.11)

29. Fowler WE, Erickson HP. 1979 Trinodular structure of fibrinogen: confirmation by both shadowing and negative stain electron microscopy. *J. Mol. Biol.* **134**, 241–249. (doi:10.1016/0022-2836(79)90034-2)

30. Williams RC. 1981 Morphology of bovine fibrinogen monomers and fibrin oligomers. *J. Mol. Biol.* **150**, 399–408. (doi:10.1016/0022-2836(81)90555-6)

31. Weisel JW, Stauffacher CV, Bullitt E, Cohen C. 1985 A model for fibrinogen: domains and sequence. *Science* **230**, 1388–1391. (doi:10.1126/science.4071058)

32. Lim BBC, Lee EH, Sotomayor M, Schulten K. 2008 Molecular basis of fibrin clot elasticity. *Structure* **16**, 449–459. (doi:10.1016/j.str.2007.12.019)

33. Tan C, Jung J, Kobayashi C, Sugita Y. 2020 A singularity-free torsion angle potential for coarse-grained molecular dynamics simulations. *J. Chem. Phys.* **153**, 044110. (doi:10.1063/5.0013089)

34. Freeman GS, Hinckley DM, Lequieu JP, Whitmer JK, de Pablo JJ. 2014 Coarse-grained modeling of DNA curvature. *J. Chem. Phys.* **141**, 165103. (doi:10.1063/1.4897649)

35. Yang Z, Mochalkin I, Doolittle RF. 2000 A model of fibrin formation based on crystal structures of fibrinogen and fibrin fragments complexed with synthetic peptides. *Proc. Natl Acad. Sci. USA* **97**, 14 156–14 161. (doi:10.1073/pnas.97.26.14156)

36. Litvinov RI, Barsegov V, Schissler AJ, Fisher AR, Bennett JS, Weisel JW, Shuman H. 2011 Dissociation of bimolecular αIIbβ3-fibrinogen complex under a constant tensile force. *Biophys. J.* **100**, 165–173. (doi:10.1016/j.bpj.2010.11.019)

37. Kamada H, Imai Y, Nakamura M, Ishikawa T, Yamaguchi T. 2013 Computational study on thrombus formation regulated by platelet glycoprotein and blood flow shear. *Microvasc. Res.* **89**, 95–106. (doi:10.1016/j.mvr.2013.05.006)

38. Ii S, Shimizu K, Sugiyama K, Takagi S. 2018 Continuum and stochastic approach for cell adhesion process based on Eulerian fluid-capsule coupling with lagrangian markers. *J. Comput. Phys.* **374**, 769–786. (doi:10.1016/j.jcp.2018.08.002)

39. Koshiyama K, Wada S. 2011 Molecular dynamics simulations of pore formation dynamics during the rupture process of a phospholipid bilayer caused by high-speed equibiaxial stretching. *J. Biomech.* **44**, 2053–2058. (doi:10.1016/j.jbiomech.2011.05.014)

40. Shigematsu T, Koshiyama K, Wada S. 2015 Effects of stretching speed on mechanical rupture of phospholipid/cholesterol bilayers: molecular

dynamics simulation. *Sci. Rep.* **5**, 15369. (doi:10.1038/srep15369)

41. Lai VK, Frey CR, Kerandi AM, Lake SP, Tranquillo RT, Barocas VH. 2012 Microstructural and mechanical differences between digested collagen-fibrin co-gels and pure collagen and fibrin gels. *Acta Biomater.* **8**, 4031–4042. (doi:10.1016/j.actbio.2012.07.010)

42. Fowler WE, Hantgan RR, Hermans J, Erickson HP. 1981 Structure of the fibrin protofibril. *Proc. Natl Acad. Sci. USA* **78**, 4872–4876. (doi:10.1073/pnas.78.8.4872)

43. Zhmurov A, Brown AEX, Litvinov RI, Dima RI, Weisel JW, Barsegov V. 2011 Mechanism of fibrin(ogen) forced unfolding. *Structure* **19**, 1615–1624. (doi:10.1016/j.str.2011.08.013)

44. Ermak DL, McCammon JA. 1978 Brownian dynamics with hydrodynamic interactions. *J. Chem. Phys.* **69**, 1352–1360. (doi:10.1063/1.436761)

45. Marsaglia G. 2003 Xorshift RNGs. *J. Stat. Softw.* **8**, 1–6. (doi:10.18637/jss.v008.i14)

46. Box GEP, Muller ME. 1958 A note on the generation of random normal deviates. *Ann. Math. Stat.* **29**, 610–611. (doi:10.1214/aoms/1177706645)

47. Ogston CM, Ogston D. 1966 Plasma fibrinogen and plasminogen levels in health and in ischaemic heart disease. *J. Clin. Pathol.* **19**, 352–356. (doi:10.1136/jcp.19.4.352)

48. Savitzky AS, Golay MJE. 1964 Smoothing and differentiation of data by simplified least squares procedures. *Anal. Chem.* **36**, 1627–1639. (doi:10.1021/ac60214a047)

49. Stylianopoulos T, Barocas VH. 2007 Volume-averaging theory for the study of the mechanics of collagen networks. *Comput. Methods Appl. Mech. Eng.* **196**, 2981–2990. (doi:10.1016/j.cma.2006.06.019)

50. Roeder BA, Kokini K, Sturgis JE, Robinson JP, Voytik-Harbin SL. 2002 Tensile mechanical properties of three-dimensional type I collagen extracellular matrices with varied microstructure. *J. Biomech. Eng.* **124**, 214–222. (doi:10.1115/1.1449904)

51. Roska FJ, Ferry JD. 1982 Studies of fibrin film. I. Stress relaxation and birefringence. *Biopolymers* **21**, 1811–1832. (doi:10.1002/bip.360210910)

52. Nelb GW, Kamykowski GW, Ferry JD. 1981 Rheology of fibrin clots. V. Shear modulus, creep, and creep recovery of fine unligated clots. *Biophys. Chem.* **13**, 15–23. (doi:10.1016/0301-4622(81)80020-8)

53. Muller MF, Ris H, Ferry JD. 1984 Electron microscopy of fine fibrin clots and fine and coarse fibrin films. *J. Mol. Biol.* **174**, 369–384. (doi:10.1016/0022-2836(84)90343-7)

54. Guimarães CF, Gasperini L, Marques AP, Reis RL. 2020 The stiffness of living tissues and its implications for tissue engineering. *Nat. Rev. Mater.* **5**, 351–370. (doi:10.1038/s41578-019-0169-1)

55. Bustamante CJ, Chemla YR, Liu S, Wnag MD. 2021 Optical tweezers in single-molecule biophysics. *Nat. Rev. Methods Primers* **1**, 25. (doi:10.1038/s43586-021-00021-6)

56. Norton DG, Fan NK, Goudie MJ, Handa H, Platt MO, Averett RD. 2017 Computational imaging analysis of

glycated fibrin gels reveals aggregated and anisotropic structures. *J. Biomed. Mater. Res. A* **105**, 2091–2198. (doi:10.1002/jbm.a.36074)

57. Veklich Y, Francis CW, White J, Weisel JW. 1998 Structural studies of fibrinolysis by electron microscopy. *Blood* **92**, 4721–4729. (doi:10.1182/blood.V92.12.4721)

58. Litvinov RI, Faizullin DA, Zuev YF, Weisel JW. 2012 The α-helix to β-sheet transition in stretched and compressed hydrated fibrin clots. *Biophys. J.* **103**, 1020–1027. (doi:10.1016/j.bpj.2012.07.046)

59. Wang Y, Kumar S, Nisar A, Bonn M, Rausch MK, Parekh SH. 2021 Probing fibrin's molecular response to shear and tensile deformation with coherent Raman microscopy. *Acta Biomater.* **121**, 383–392. (doi:10.1016/j.actbio.2020.12.020)

60. Mickel W, Münster S, Jawerth LM, Vader DA, Weitz DA, Sheppard AP, Mecke K, Fabry B, Schröder-Turk GE. 2008 Robust pore size analysis of filamentous networks from three-dimensional confocal microscopy. *Biophys. J.* **95**, 6072–6080. (doi:10.1529/biophysj.108.135939)

61. Xia J, Cai LH, Wu H, MacKintosh FC, Weitz DA. 2021 Anomalous mechanics of Zn^{2+}-modified fibrin networks. *Proc. Natl Acad. Sci. USA* **118**, e2020541118. (doi:10.1073/pnas.2020541118)

62. Wolberg AS, Rosendaal FR, Weitz JI, Jaffer IH, Agnelli G, Baglin T, Mackman N. 2015 Venous thrombosis. *Nat. Rev. Disease Primers* **1**, 15006. (doi:10.1038/nrdp.2015.6)

63. Chernysh IN, Nagaswami C, Kosolapova S, Peshkova AD, Cuker A, Cines DB, Cambor CL, Litvinov RI, Weisel JW. 2020 The distinctive structure and composition of arterial and venous thrombi and pulmonary emboli. *Sci. Rep.* **10**, 5112. (doi:10.1038/s41598-020-59526-x)

64. Janmey PA, Winer JP, Weisel JW. 2009 Fibrin gels and their clinical and bioengineering applications. *J. R. Soc. Interface* **6**, 1–10. (doi:10.1098/rsif.2008.0327)

65. Sivaraj D. 2021 Hydrogel scaffolds to deliver cell therapies for wound healing. *Front. Bioeng. Biotechnol.* **9**, 660145. (doi:10.3389/fbioe.2021.660145)

66. Rana A, Westein E, Niego B, Hagemeye CE. 2019 Shear-dependent platelet aggregation: mechanisms and therapeutic opportunities. *Font. Cardiovasc. Med.* **6**, 141. (doi:10.3389/fcvm.2019.00141)

67. Neeves KB, Illing DA, Diamond SL. 2010 Thrombin flux and wall shear rate regulate fibrin fiber deposition state during polymerization under flow. *Biophys. J.* **98**, 1344–1352. (doi:10.1016/j.bpj.2009.12.4275)

68. Gersh KC, Edmondson KE, Weisel JW. 2010 Flow rate and fibrin fiber alignment. *J. Thromb. Haemost.* **8**, 2826–2828. (doi:10.1111/j.1538-7836.2010.04118.x)

69. Campbell RA, Aleman MM, Gray LD, Falvo MR, Wolberg AS. 2010 Flow profoundly influences fibrin network structure: implications for fibrin formation and clot stability in haemostasis. *Thromb. Haemost.* **104**, 1281–1284. (doi:10.1160/TH10-07-0442)

70. Whittaker P, Przyklenk K. 2009 Fibrin architecture in clots: a quantitative polarized light microscopy analysis. *Blood Cells Mol. Dis.* **42**, 51–56. (doi:10.1016/j.bcmd.2008.10.014)

71. Varjú I, Sótonyi P, Machovich R, Szabó L, Tenekedjiev K, Silva MMCG, Longstaff, C, Kolev K. 2011 Hindered dissolution of fibrin formed under mechanical stress. *J. Thromb. Haemost.* **9**, 979–986. (doi:10.1111/j.1538-7836.2011.04203.x)

72. Weiss HJ, Turitto VT, Baumgartner HR. 1986 Role of shear rate and platelets in promoting fibrin formation on rabbit subendothelium. Studies utilizing patients with quantitative and qualitative platelet defects. *J. Clin. Invest.* **78**, 1072–1082. (doi:10.1172/JCl112663)

73. Tijburg PN, Ijsseldijk MJ, Sixma JJ, de Groot PG. 1991 Quantification of fibrin deposition in flowing blood with peroxidase-labeled fibrinogen. High shear rates induce decreased fibrin deposition and appearance of fibrin monomers. *Arterioscler. Thromb.* **11**, 211–220. (doi:10.1161/01.ATV.11.2.211)

74. Kamada H, Imai Y, Nakamura M, Ishikawa T, Yamaguchi T. 2012 Computational analysis on the mechanical interaction between a thrombus and red blood cells: possible causes of membrane damage of red blood cells at microvessels. *Med. Eng. Phys.* **34**, 1411–1420. (doi:10.1016/j.medengphy.2012.01.003)

75. Rack K, Huck V, Hoore M, Fedosov DA, Schneider SW, Gompper G. 2017 Margination and stretching of von Willebrand factor in the blood stream enable adhesion. *Sci. Rep.* **7**, 14278. (doi:10.1038/s41598-017-14346-4)

76. Ye H, Shen Z, Li Y. 2019 Interplay of deformability and adhesion on localization of elastic micro-particles in blood flow. *J. Fluid Mech.* **861**, 55–87. (doi:10.1017/jfm.2018.89)

77. Takeishi N, Rosti ME, Imai Y, Wada S, Brandt L. 2019 Haemorheology in dilute, semi-dilute and dense suspensions of red blood cells. *J. Fluid Mech.* **872**, 818–848. (doi:10.1017/jfm.2019.393)

78. Takeishi N, Imai Y, Wada S. 2019 Capture event of platelets by bolus flow of red blood cells in capillaries. *J. Biomech. Sci. Eng.* **14**, 1–10. (doi:10.1299/jbse.18-00535)